ACS MATERIALS LETTERS

www.acsmaterialsletters.org

PERSPECTIVE

Emerging Electrocatalytic Textile Electrodes for Highly Efficient Alkaline Water Electrolysis

Published as part of ACS Materials Letters virtual special issue "Materials for Water Splitting".

Jeongmin Mo,[¶] Wondo Choi,[¶] Hyaemin Kim, Jaesung Lyu, Cheong Hoon Kwon, Dongsoo Yang,* and Jinhan Cho*

Cite This: *ACS Materials Lett.* 2024, 6, 3133−3160

ABSTRACT: Alkaline water electrolysis using non-noble electrocatalysts represents a sustainable method of hydrogen production, but optimizing/maximizing its performance still remains a challenge. While extensive research has focused mainly on the synthesis and design of electrocatalysts, less attention has been given to the structural and interfacial design of electrodes, which critically affects the water-splitting performance. Of particular importance is the interfacial controlled host electrode, which serves as a uniform electrocatalyst reservoir through interfacial interactions and a highly conductive current collector. Its porous structure, in addition to electrocatalyst size and host-electrocatalyst interface, significantly influences the total active surface area and operational stability. Here, we review recent advances in alkaline water electrolysis, highlighting the crucial role of interfacial interactions between host electrode and electrocatalysts, and among adjacent electrocatalysts, as well as the structural design of host electrode. Additionally, we explain how these interactions significantly contribute to operational stability. Commercialization challenges are also discussed.

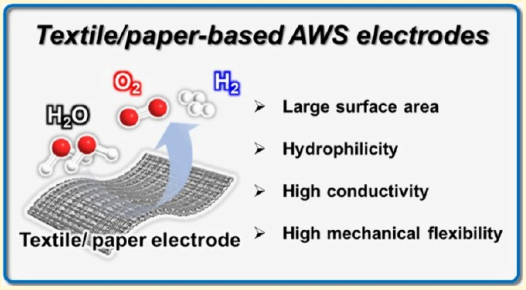

Looming threats of unpredictable climate change, global warming, and energy insecurity, amplified by an ever-growing population, require the immediate expansion of renewable energy sources and efficient energy storage solutions.[1−4] Although various renewable resources involving wind, solar, and geothermal energy have undergone rapid development and advancement, their inherent dependence on weather and location poses a persistent challenge: their fluctuating output hinders their ability to serve as reliable energy sources.[5,6] Against this backdrop, hydrogen gas stands out as the ultimate clean fuel with high energy density and efficient conversion potential to power future human societies.[1−7] However, current production methods, which rely heavily on fossil-fueled steam methane reforming (∼78%) and coal gasification (∼18%), cause environmental damage through significant carbon dioxide emissions.[8−10]

To address this hydrogen production issue, electrocatalytic water-splitting has emerged as an alternative means for sustainable hydrogen production. Powered by electricity, this technology splits water into hydrogen and oxygen, driving the hydrogen evolution reaction (HER) at the cathode and the oxygen evolution reaction (OER) at the anode.[11,12] Notably, this process frees us from fossil fuels while producing oxygen as a byproduct. To this end, considerable research has focused on the development of efficient and cost-effective HER and OER electrocatalysts, primarily non-noble metal composites (Ni, Co, Fe, and/or Mo) as affordable alternatives to noble and rare metals (Pt, Ir and Ru), which limit large-scale electrolysis applications due to their high cost despite their excellent water-splitting efficiency.[13−17] In particular, since the alkaline water-splitting (AWS) among various water-splitting systems can effectively produce hydrogen using the non-noble metal composite electrocatalysts, unlike the acid proton membrane (PEM) system using the aforementioned noble and rare metal electrocatalysts, the AWS system has been considered as one of the most attractive water-splitting technologies for green hydrogen production.[18,19] However, the commercial AWS system lags behind PEM electrolyzers in terms of operating current density, typically capping out at <500 mA cm^{-2}.[19−21]

Received: March 26, 2024
Revised: May 16, 2024
Accepted: May 24, 2024
Published: June 20, 2024

https://doi.org/10.1021/acsmaterialslett.4c00659
ACS Materials Lett. 2024, 6, 3133−3160

Therefore, increasing AWS current density to ~1000 mA cm^{-2} with long-term durability is critical to enable rapid, industrial-scale hydrogen production.[22,23]

To enhance the hydrogen production efficiency of AWS system, intensive research efforts have been concentrated on developing HER and OER electrodes with low overpotentials (*this excess potential is necessary to overcome the energy barrier of electrochemical water-splitting reaction*) and long-term durability at high current densities using diverse non-noble metal electrocatalysts, such as 3*d* oxides,[24−27] phosphides,[28−31] nitrides,[32−35] and sulfides.[36−39] For instance, Hao et al. reported remarkable electrocatalytic performance for both OER and HER using 3*d* oxides (Ni_5Co_3Mo−OH nanosheets) with impressive bifunctional properties.[40] These nanosheets achieved an overpotential of ~304 mV at 100 mA cm^{-2} for OER and ~52 mV at 10 mA cm^{-2} for HER. Notably, the resulting overall water-splitting device exhibited a low cell voltage of 1.60 V at 100 mA cm^{-2} and high stability for 100 h at the same current density. Luo et al. also reported that Mo-doped sulfide/phosphide (Mo−Ni_3S_2/Ni_xP_y) could be synthesized onto 3D nickel foam through a solvothermal process, which exhibited an extremely low overpotential of 238 mV at the current density of 50 mA cm^{-2} for OER.[41] Moreover, the bifunctional overall water-splitting device required a significantly low cell voltage of 1.46 V to achieve the current density of 10 mA cm^{-2}, with durability for over 72 h. Recently, Li et al. demonstrated overall water-splitting device using porous Co−P electrocatalysts-decorated Co foam. This device achieved a low cell voltage of 1.98 V at a high current density of 2000 mA cm^{-2}, demonstrating its excellent efficiency.[42] In addition, it exhibited enhanced durability, maintaining the stable operation for 4000 h at a current density of 1000 mA cm^{-2}.

Alkaline water electrolysis using non-noble electrocatalysts represents a sustainable method of hydrogen production, but optimizing/maximizing its performance still remains a challenge.

Applied current density also plays an important role in determining the electrocatalytic performance (including overpotentials, active sites of electrocatalysts, electron transfer at the interface between electrocatalysts and host electrode, mass transfer process, and mechanical/chemical stability) of the AWS system.[22,43,44] In particular, with increasing the applied potential, the chemical structure of transition metal-based electrocatalysts gradually deforms, which has a critical effect on the electrocatalytic performance and operational stability of the electrodes.[45,46] Various approaches to regulate this deformation and improve the electrocatalytic performance have been reported. For example, Chen et al., reported that tertiary metal catalysts such as FeCoNi are highly advantageous compared to single or binary structured electrocatalysts in reliably generating a highly active β-NiOOH phase, which is considered to be the most active structure of NiOOH phases at high current densities.[47] However, despite these advances in enhancing the electrocatalytic performance of electrodes, challenges still remain in further reducing overpotentials and in significantly increasing the operational stability at elevated current densities.

As another alternative, highly porous 3D host electrodes (or current collectors) such as textile or paper host electrodes can offer a pathway to boost the electrocatalytic performance of HER and OER electrodes. Compared to conventional Ni foam or carbon cloth, these host electrodes enhance mass transport and facilitate deposition of larger electrocatalyst amounts.[48] Sahasrabudhe et al. demonstrated this by electrodepositing NiMo for HER and NiFe for OER onto a Ni cellulose paper prepared through chemical reduction of Ni ions.[49] These electrodes reached exceptional activities, with overpotentials of ~32 mV at 10 mA cm^{-2} for NiMo and ~240 mV at 50 mA cm^{-2} for NiFe. The device also exhibited robust stability exceeding 200 h at 10 mA cm^{-2}. However, in most cases, chemical reduction deposition generally generates the insulating organic impurities within electrocatalytic layers, and furthermore struggles with producing highly uniform coatings and structures due to limited control over interfacial interactions between the host and deposited components.[50,51] In addition, the contact resistance occurring at the interface between electrocatalysts and host electrode, as well as the electrical resistances of electrocatalysts and host electrode themselves, have a dominant effect on the total internal resistance of the water-splitting electrodes, which is closely related to the overpotentials of overall water-splitting electrodes. That is, most of the approaches reported to date have much difficulty in controlling the interfacial interactions between electrocatalysts and host electrode as well as reducing the internal resistance of electrocatalysts, thus resulting in

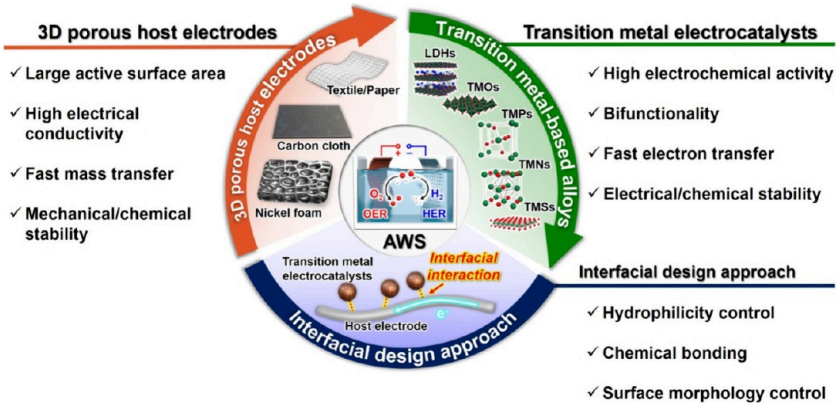

Figure 1. Schematic illustration of the interfacial design strategies for 3D structured electrodes utilized in alkaline water-splitting applications, incorporating various transition metal electrocatalysts.

https://doi.org/10.1021/acsmaterialslett.4c00659
ACS Materials Lett. 2024, 6, 3133−3160

unsatisfactory electrical conductivity, uneven deposition, and poor interfacial adhesion of electrocatalysts on the 3D porous host electrode. To put it bluntly, the interfacial interaction between the 3D porous substrate and the electrocatalytic layer has not been thoroughly studied. Although unfavorable interfacial interaction causes the detachment of electrocatalysts from host electrode (by large amounts of hydrogen and oxygen bubble gases) at high current densities as well as the agglomeration and/or nonuniformity (i.e., decrease of accessible electrocatalytic area),[52−54] little experimental consensus has existed on the interfacial design that can significantly improve the electrocatalytic performance of AWS electrodes. Therefore, the development of unique approach for efficiently resolving such critical issues has been strongly demanded for commercially available high-performance AWS electrodes.

A number of reviews on the alkaline water-splitting reaction have been summarized to provide a comprehensive overview of the electrolytic water-splitting mechanism and the progress in the preparation of various non-noble metal electrocatalysts with remarkable electrocatalytic activity and operational stability for HER and OER.[55−62] However, to the best of our knowledge, the aforementioned other critical factors involving the interfacial interactions, the structural design of the host electrodes, and the uniformity of the electrocatalyst coating on the host electrode have not been addressed in the water-splitting-related reviews or perspective papers.

In this perspective, we introduce interfacial design approaches and recent advances in 3D porous AWS electrodes (Figure 1). Although this underscores the importance of addressing challenges pertaining to membranes within water electrolysis systems as well as electrocatalytic electrodes,[63−65] we focus on the issues related to securing and enhancing the water-splitting activity and stability of the electrodes. The main focus of this perspective is to discuss significant challenges in the area of electrocatalysts and 3D porous electrodes, including textile and/or paper-based AWS electrodes, and to present potential approaches to overcome critical obstacles to the development of high-performance AWS electrodes with low overpotentials and long-term operation. First, we briefly describe the basic mechanism of the electrochemical water-splitting reaction, and then introduce various electrocatalysts applicable to AWS electrodes, particularly self-supported, and 3D porous host electrodes prepared by different approaches. We also present the recent advances in AWS electrodes using a variety of interfacial interaction-induced assembly approaches. In particular, we discuss in detail how the interfacial control and design of electrocatalysts and host electrodes can effectively improve the charge transfer kinetics within the HER and OER electrodes and their operational stability. Finally, we present a brief perspective on the direction of optimized interfacial assembly for the realization of high-performance AWS electrodes.

Electrolytic water-splitting in AWS involves two pivotal half reactions: HER at the cathode and OER at the anode. The corresponding half-cell reactions and overall reaction are described as follows (1−3):[7,59]

$$\text{HER: } 4H_2O + 4e^- \rightarrow 2H_2 + 4OH^-,\ E^\circ = -0.828\ \text{V} \quad (1)$$

$$\text{OER: } 4OH^- \rightarrow O_2 + 2H_2O + 4e^-,\ E^\circ = +0.401\ \text{V} \quad (2)$$

This review outlines recent advances in alkaline water electrolysis, highlighting the crucial role of interfacial interactions between host electrode and electrocatalysts, and among adjacent electrocatalysts, as well as the structural design of host electrode.

$$\text{Overall reaction: } 2H_2O \rightarrow 2H_2 + O_2,\ E^\circ = +1.230\ \text{V} \quad (3)$$

Although the theoretical potential required for electrolytic water-splitting is 1.230 V (25 °C, 1 atm), the water-splitting reaction for commercial electrolysis occurs at cell potential of 1.8 to 2.0 V, which is about 0.55 to 0.77 higher than the theoretical value (1.230 V).[66−68] Thus, for actual water electrolysis, the extra energy, called overpotential, must be supplied to the cell for actual water electrolysis due to the presence of various energy barriers such as activation energy (required to initiate the electrochemical reaction), ohmic resistances (the resistances of electrode, electrolyte, and separator encountered by ions and electrons), concentration gradients (due to ion concentration at the electrode surfaces), and mass transport (by limitations in the transport of reactants to the electrode or the removal of products from the electrode surface).[69,70] In this regard, one of major challenges in water-splitting reaction is to develop highly efficient electrocatalysts and electrodes to minimize the overpotentials caused by various factors (more details will be given in the latter part).

Electrolytic water-splitting involves two pivotal half reactions: HER at the cathode and OER at the anode.

In addition, the HER mechanisms are strongly dependent on the surrounding electrolyte, as demonstrated by following three different mechanisms (4)-(6):[71−73]

$$\text{Volmer reaction: } H_2O + M + e^- \rightarrow MH_{ads} + OH^- \quad (4)$$

$$\text{Heyrovsky reaction: } MH_{ads} + H_2O + e^- \rightarrow M + OH^- + H_2 \quad (5)$$

$$\text{Tafel reaction: } 2MH_{ads} \rightarrow 2M + H_2 \quad (6)$$

The initiation of HER involves an initial step, known as the Volmer reaction, wherein the adsorption of hydrogen (H_{ads}) occurs on the metal surface (M). In this case, the degree of H_{ads} coverage on the metal surface significantly influences its interaction with different reactants (H_2O or H_{ads}), thereby dictating different pathways for H_2 molecules (Figure 2**a**, **b**).[74,75] Specifically, a low H_{ads} coverage tends to favor the Volmer-Heyrovsky mechanism, while a high H_{ads} coverage favors the Volmer−Tafel mechanism.

To delve deeper into these mechanisms, analysis of the Tafel plot derived from the polarization curve can be insightful. Ideally, the Tafel plot reveals the intrinsic properties of the electrocatalysts and sheds light on the HER mechanisms at active sites. In AWS systems, the Tafel slopes of 118, 39, and 29 mV dec^{-1} correspond to the Volmer, Heyrovsky, and Tafel steps in HER, respectively, indicating their role as the rate-

https://doi.org/10.1021/acsmaterialslett.4c00659
ACS Materials Lett. 2024, 6, 3133−3160

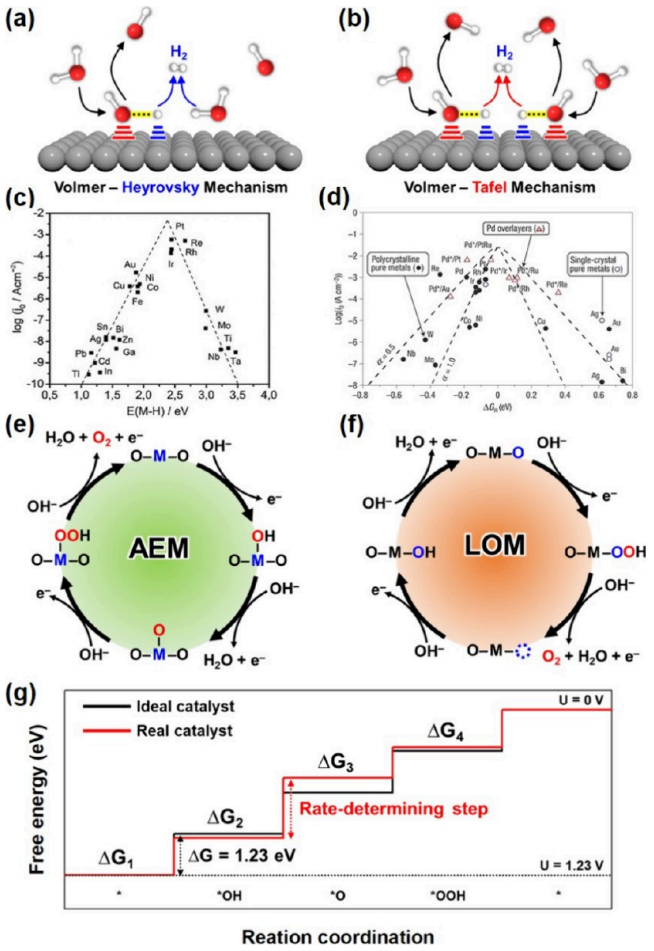

Figure 2. Schematic diagram of the (a) Volmer-Heyrovsky and (b) Volmer−Tafel mechanism on a catalyst surface for HER. (c) Experimental "volcano plot" derived by Trasatti. For each metal surface, the logarithm of the exchange current density j_0 is plotted against M-H bond energy. Reprinted with permission from ref 80. Copyright 2016, Wiley-VCH. (d) Volcano plot for the HER for various pure metals and metal overlayers. The experimentally logarithm of the exchange current density j_0 was plotted against ΔG_H values calculated using DFT calculations. Reprinted with permission from ref 82. Copyright 2006, Springer Nature. Conventional (e) AEM and (f) LOM mechanisms in alkaline media. (g) Gibbs free energies for ideal and actual catalyst.

determining steps (RDS).[62] More specifically, the Tafel eq (eq 7) further quantifies this relationship.[76]

$$\eta = b\log|j| + a \tag{7}$$

where η is the overpotential, b is the Tafel slop value, j is the current density, and a is a constant. Notably, at zero overpotential ($\eta = 0$), the current density (j) becomes the exchange current density (j_o), reflecting the intrinsic charge transfer between electrocatalysts and the reactants. Smaller Tafel slopes indicates faster reaction kinetics, while higher j_o values suggest lower driving force needed for the reaction to proceed.[77,78] Therefore, electrocatalysts with low overpotentials, high exchange current densities, and small Tafel slopes stand out as excellent electrocatalysts for HER.

As shown in Figure 2c, Trasatti's iconic "volcano plot" reveals a crucial relationship between the logarithm of exchange current density (log j_o) and the metal−hydrogen (M-H) bond strength for HER in acidic media.[79,80] This curve serves as a guiding principle, highlighting metals with an optimal M-H bond strength (neither too strong nor too weak) for efficient HER, aligning with the Sabatier principle.[81] Following Trasatti's groundbreaking work, researchers have continuously refined this approach to establish robust descriptors for diverse HER catalysts. In 2006, Nørskov's group pushed the boundaries by correlating experimentally measured HER j_o with the free energy of hydrogen adsorption (ΔG_{H^*}) using density functional theory (DFT) calculations (Figure 2d).[82] This pioneering work offered a powerful theoretical framework for catalyst design. Building upon these advancements, Yan's group further extended the concept by establishing a similar correlation between HER j_o and calculated hydrogen binding energy in alkaline media, demonstrating the versatility of this approach across different electrolytes.[83] Although these volcano plots provide a valuable roadmap for HER catalyst design, their reliance on a single descriptor (M-H bond strength) can sometimes limit their accuracy. Numerous other factors influence HER activity, prompting the introduction of additional descriptors such as pH value, water adsorption, dissociation energy, and adsorption strength of OH^- and d-band center.[84] These comprehensive descriptors offer a more nuanced understanding of catalyst performance in water-splitting systems.

Compared to HER, the OER presents a more complicated mechanism due to its nature as a four-electron−proton coupled transfer reaction involving multiple intermediates.[85,86] This inherent complexity of OER translates into a higher overpotential than HER to overcome kinetic barriers. In AWS, two typical OER mechanisms are recognized as follows: the adsorbate evolving mechanism (AEM) and the lattice oxygen mechanism (LOM).[87−89] Each mechanism is described in Figure 2e, f and expressed by the following eqs 8-(15):

> Compared to HER, the OER presents a more complicated mechanism due to its nature as a four-electron-proton coupled transfer reaction involving multiple intermediates.

AEM reaction:

$$O\text{-}M\text{-}O + OH^- \rightarrow O\text{-}M(OH)_{ads}\text{-}O + e^- \tag{8}$$

$$O\text{-}M(OH)_{ads}\text{-}O + OH^- \rightarrow O\text{-}M(O)_{ads}\text{-}O + H_2O + e^- \tag{9}$$

$$O\text{-}M(O)_{ads}\text{-}O + OH^- \rightarrow O\text{-}M(OOH)_{ads}\text{-}O + e^- \tag{10}$$

$$O\text{-}M(OOH)_{ads}\text{-}O + OH^- \rightarrow O\text{-}M\text{-}O + O_2 + H_2O + e^- \tag{11}$$

LOM reaction:

$$O\text{-}M\text{-}O + OH^- \rightarrow O\text{-}M\text{-}O(OH)_{ads} + e^- \tag{12}$$

$$O\text{-}M\text{-}O(OH)_{ads} + OH^- \rightarrow O\text{-}M\text{-}O_v + O_2 + H_2O + e^- \tag{13}$$

$$O\text{-}M\text{-}O_v + OH^- \rightarrow O\text{-}M\text{-}OH + e^- \tag{14}$$

$$O\text{-}M\text{-}OH + OH^- \rightarrow O\text{-}M\text{-}O + H_2O + e^- \tag{15}$$

Both these two mechanisms (AEM and LOM) start with the adsorption of OH^- ions onto the active site. In the AEM, a

https://doi.org/10.1021/acsmaterialslett.4c00659
ACS Materials Lett. 2024, 6, 3133−3160

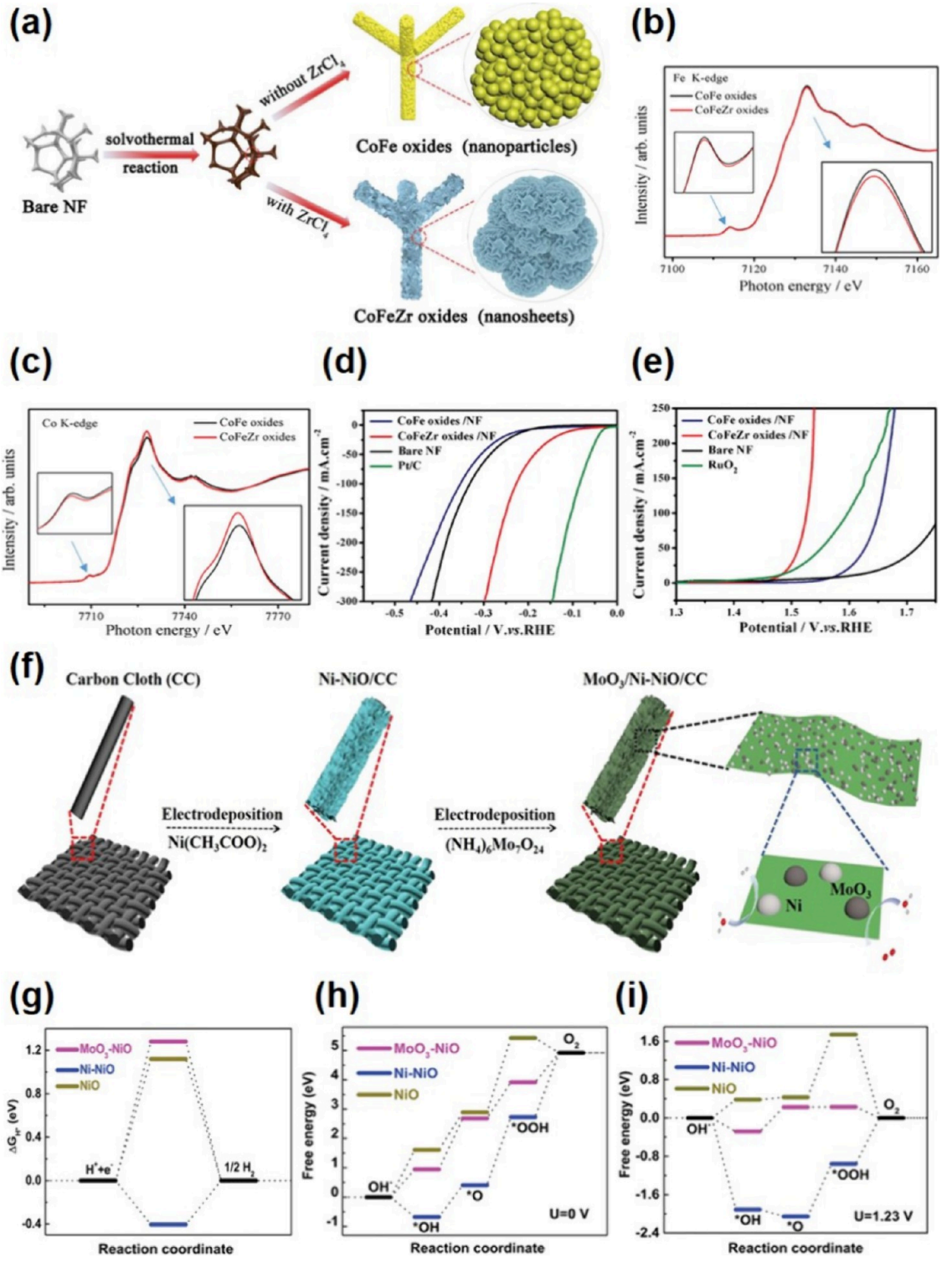

Figure 3. (a) Schematic illustration for in situ growth of CoFe oxides and CoFeZr oxides on the nickel foam. Reprinted with permission from ref 101. Copyright 2019, Wiley-VCH. (b) Fe K-edge XANES spectra of CoFe oxides and CoFeZr oxides. Reprinted with permission from ref 101. Copyright 2019, Wiley-VCH. (c) Co K-edge XANES spectra of CoFe oxides and CoFeZr oxides. Reprinted with permission from ref 101. Copyright 2019, Wiley-VCH. (d) The polarization curves of HER on CoFe oxides/NF (Nickel foam), CoFeZr oxides/NF, Bare NF, and Pt/C in 1 M KOH. Reprinted with permission from ref 101. Copyright 2019, Wiley-VCH. (e) The polarization curves of OER on CoFe oxides/NF, CoFeZr oxides/NF, Bare NF, and RuO_2 in 1 M KOH. Reprinted with permission from ref 101. Copyright 2019, Wiley-VCH. (f) Schematic illustration for the fabrication of MoO_3/Ni-NiO on carbon cloth. Reprinted with permission from ref 102. Copyright 2020, Wiley-VCH. (g) Gibbs free energy diagram of the HER process of NiO, Ni-NiO, and MoO_3−NiO surface. Reprinted with permission from ref 102. Copyright 2020, Wiley-VCH. Gibbs free energy diagram of the OER process (h) at U = 0 V and (i) U = 1.23 V for NiO, Ni-NiO, and MoO_3−NiO heterostructures. Reprinted with permission from ref 102. Copyright 2020, Wiley-VCH.

https://doi.org/10.1021/acsmaterialslett.4c00659
ACS Materials Lett. 2024, 6, 3133−3160

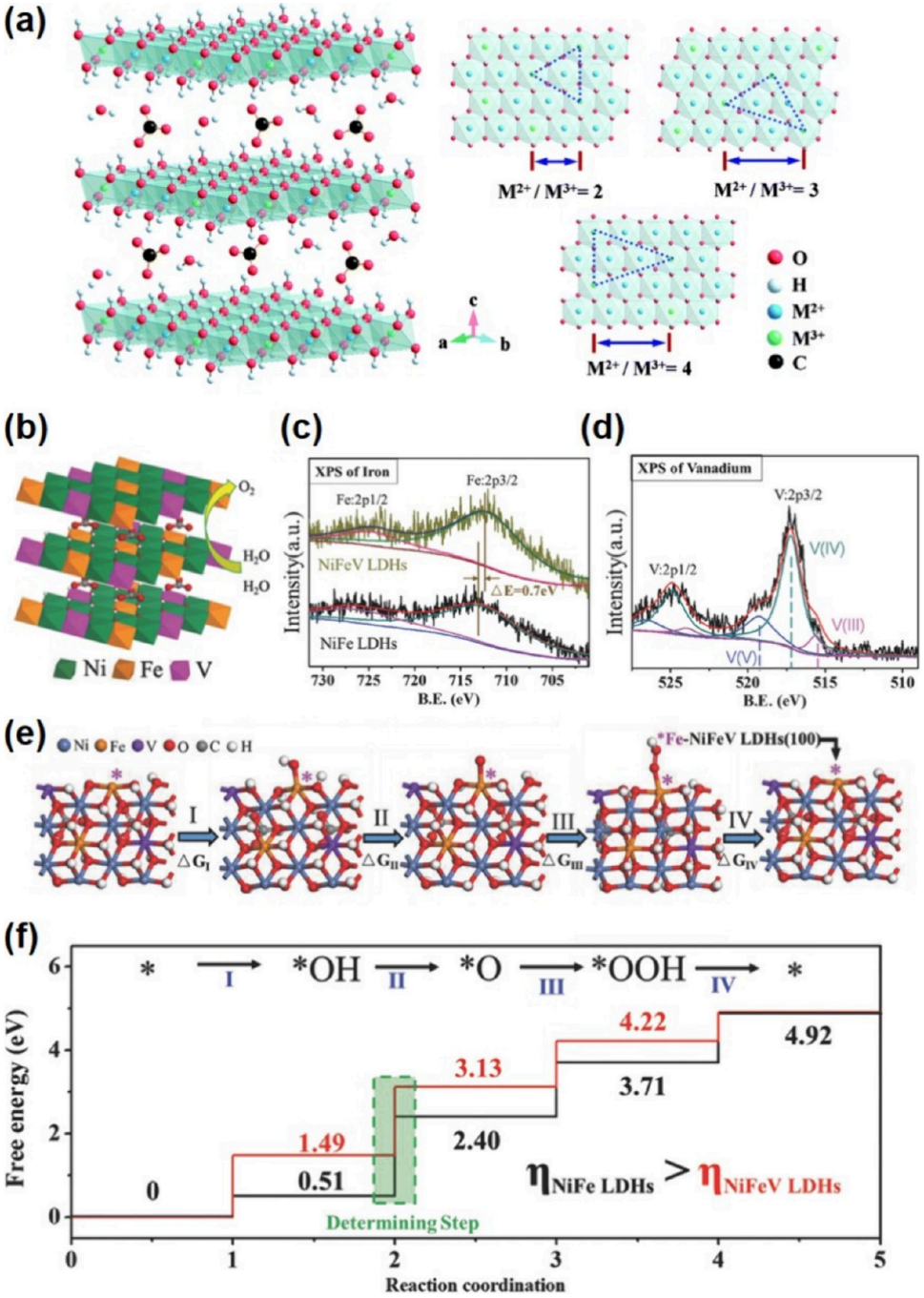

Figure 4. (a) The idealized structure of carbonate-intercalated LDHs with different M^{2+}/M^{3+} molar ratios showing the metal hydroxide octahedra stacked along the crystallographic *c*-axis, as well as water and anions present in the interlayer region. Reprinted with permission from ref 103. Copyright 2014, The Royal Society of Chemistry. (b) The schematic diagram of NiFeV LDHs structure. Reprinted with permission from ref 109. Copyright 2018, Wiley-VCH. (c) The high resolution XPS spectra of Fe in the NiFe LDHs and NiFeV LDHs nanosheets array. Reprinted with permission from ref 109. Copyright 2018, Wiley-VCH. (d) The high resolution XPS spectra of V in the NiFeV LDHs nanosheets array. Reprinted with permission from ref 109. Copyright 2018, Wiley-VCH. (e) Proposed 4e-mechanism of OER on NiFeV LDHs for DFT+U calculation. The Fe ion (*) in the (100) crystal plane was the active site. ΔG stands for the reaction Gibbs free energy. Reprinted with permission from ref 109. Copyright 2018, Wiley-VCH. (f) Gibbs free energy diagram for the four steps of OER on the NiFe LDHs (black line) and NiFeV LDHs (red line). The top was the brief 4e-mechanism of OER. The green box step was the determining step and η was stand for overpotential. The lower activation Gibbs free energy of NiFeV LDHs predicts more favorable OER kinetics. Reprinted with permission from ref 109. Copyright 2018, Wiley-VCH.

metal itself serves as the redox center, boasting metallic properties near the Fermi level. As the reaction progresses, various intermediates (*OH, *O, *OOH) bond to the metal surface (M), which remains remarkably stable as it merely facilitates OER without being consumed. In contrast, LOM utilizes oxygen as the redox center, exhibiting oxygen-like electronic characteristics around the Fermi level. Since lattice oxygen serve as the reaction center, it forms $(O-O)_{2p}$ hybridized bonds and oxygen vacancies (O_v) when it disappears during OER. These $(O-O)_{2p}$ bonds contribute to

https://doi.org/10.1021/acsmaterialslett.4c00659
ACS Materials Lett. 2024, 6, 3133−3160

superior catalytic activity compared to AEM. However, the repeated attachment and detachment of lattice oxygen to the catalyst surface can lead to structural instability, often termed the "instantaneous dissolution mechanism".

These interwoven mechanisms highlight a crucial point: OER necessitates a continuous oxidation−reduction cycle at the catalytic site, beginning with the adsorption of water/hydroxide ions and culminating in the formation of a dioxygen molecule. This implies significant structural rearrangements at the surface, shaping the electrocatalytically active structure.[90] Therefore, understanding how electrocatalysts interact with intermediates holds the key to enhancing the overall OER performance. In particular, the Gibbs free energy change associated with each reaction step depends on the variation in the binding energies of the intermediates.[91,92] These deviations arise due to irregularities in the adsorption energies of intermediate species on different electrocatalysts (Figure 2**g**). In this case, identifying the reaction step with the highest free energy change serves as the rate-determining step (RDS). Given the complex nature of electrocatalysts and their sensitivity, the identification of the RDS is of great importance. Therefore, it provides critical insight for electrocatalyst design aimed at optimizing OER efficiency.

The intrinsic electron structures of *3d*-transition metals (Ni, Fe, Co, Mn, Mo, Cu, etc.) play a significant role in both HER and OER in alkaline media, influencing electron−proton transfer rates and intermediate adsorption/desorption behavior. Although these single transition metal electrocatalysts are promising, their electrocatalytic activity is inherently limited compared to noble metals, hindering practical applications. To address this, considerable research has focused on transition metal-based composites − (hydro)oxides, phosphides, nitrides, sulfides, and others−as promising AWS electrocatalysts. In these composites, strategically chosen heteroatoms can reshape the electron structures, creating abundant active sites, lowering energy barriers, and ultimately increasing water-splitting reaction rates.[93−95] Furthermore, the interfaces between or among different transition metal-based composites could serve as active sites, optimizing the energy barriers of overall water splitting and inducing differential charge densities to enhance reaction kinetics and activities.[41,102]

The following sections provide an overview of various transition metal-based composites that can be used as HER and OER electrocatalysts in alkaline media, with particular emphasis on lowering the overpotentials through atomic structural modification.

Earth-abundant transition metal oxides (TMOs) have emerged as promising electrocatalysts for water electrolysis due to their remarkable chemical stability and adjustable electronic structures. Recent research has explored various oxides such as Co_3O_4,[96] $CoFe_2O_4$,[97] NiO,[98] MnO_2,[99] and MoO_3,[100] demonstrating their effectiveness in water-splitting. For instance, Huang et al. developed zirconium-regulated $CoFe_2O_4$ nanosheets on nickel foam through solvothermal synthesis (Figure 3a).[101] This approach led to significant enhancements in electrocatalytic efficiency for both HER and OER. Through precise control over their active site density, chemical composition, and electronic structure, they demonstrated that the incorporation of Zr could enhance the intrinsic activity of $CoFe_2O_4$ nanosheets. As a result, the formed water-splitting electrode exhibited impressively low overpotentials: 104 mV at 10 mA cm^{-2} for HER and 282 mV at 50 mA cm^{-2} for OER in 1 M KOH (Figure 3**b-e**). Li et al. also reported the fabrication of amorphous NiO nanosheets electrocatalysts with MoO_3 and Ni nanoparticles (MoO_3/Ni-NiO) on carbon cloth using a sequential electrodeposition strategy (Figure 3f).[102] Through experimental analysis and DFT simulations, they found that the Ni-NiO composite played a significant role in facilitating the HER due to its favorable bonding strength with hydrogen reactants. Simultaneously, the MoO_3−NiO heterostructure was observed to optimize the energy barriers for the formation of adsorbed oxygen species (O_{ads}) as the RDS for OER (Figure 3**g-i**). These optimized TMOs-based electrocatalysts demonstrated low overpotentials of 62 mV at 10 mA cm^{-2} for HER and 347 mV at 100 mA cm^{-2} for OER.

In addition to these oxides, layered double hydroxides (LDHs) have emerged as another promising class of electrocatalysts for water-splitting. These intriguing 2D materials possess a distinctive supramolecular structure, featuring positively charged brucite-like host layers interspersed with exchangeable charge-balancing interlayer anions (Figure 4a).[103] Their formula, $[M^{2+}_{1-x}M^{3+}_{x}(OH)_2]\ [A_{x/n}{}^{n-}\cdot mH_2O]$, reflects their tunability: the ratio of M^{2+}/M^{3+} and the nature of the metal cations or interlayer anions can be easily adjusted to tailor their electronic structures. Taking advantage of this versatility, researchers have actively explored various strategies such as surface distortion, defect engineering, and ion regulation to optimize LDHs for electrocatalytic water-splitting applications.[104−107] For example, Zhou et al. demonstrated the enhancement of electrochemical surface area and wettability by introducing Fe-doped Ni/Co hydroxide nanosheets through a cation-exchange reaction.[108] This improvement was observed despite maintaining a similar Ni/Fe ratio compared to conventional NiFe-LDH nanosheets. Furthermore, Sun's group employed a one-step hydrothermal method to synthesize vanadium doped NiFe LDHs nanosheets array on nickel foam (Figure 4b).[109] Their study highlighted the role of vanadium doping in enhancing the catalytic activities of Fe sites through electronic interactions between Fe and V atoms. This approach induced the more facile electron transfer, and further increased the active sites, as confirmed by X-ray photoelectron spectroscopy (XPS) analysis and DFT with a Hubbard U correction ((DFT)+U) simulation (Figure 4**c-f**). These results highlight how engineering LDH nanostructures can significantly increase defects and active sites, offering a promising approach to enhancing electrocatalytic activity. However, a significant challenge remains: most transition metal oxides and hydroxides suffer from inherently low electrical conductivity, which limits the overall efficiency of AWS systems.

Another strategy to overcome the limitations of transition metal oxide catalysts for water-splitting is to manipulate their band gap and Fermi level through nonmetallic element doping. In this regard, elements such as phosphorus, nitrogen, and sulfur have emerged as promising nonmetallic dopants. In particular, pioneering work by Liu and Rodriguez in 2005 used DFT calculations to identify Ni_2P (001) as a highly effective catalyst for HER.[110] They attributed its success to the "ensemble effect," in which P atoms moderate the binding energies of reactants and the catalyst, preventing overbinding and under-binding for optimal activity. This paved the way for numerous experimental explorations of nanoscale transition metal phosphides (TMPs) for high-performance AWS. In 2013, Zhang's group first synthesized nanoporous FeP nanosheets via an anion-exchange route, achieving impressive electrocatalytic activity and low Tafel slopes.[111] Around the

https://doi.org/10.1021/acsmaterialslett.4c00659
ACS Materials Lett. 2024, 6, 3133−3160

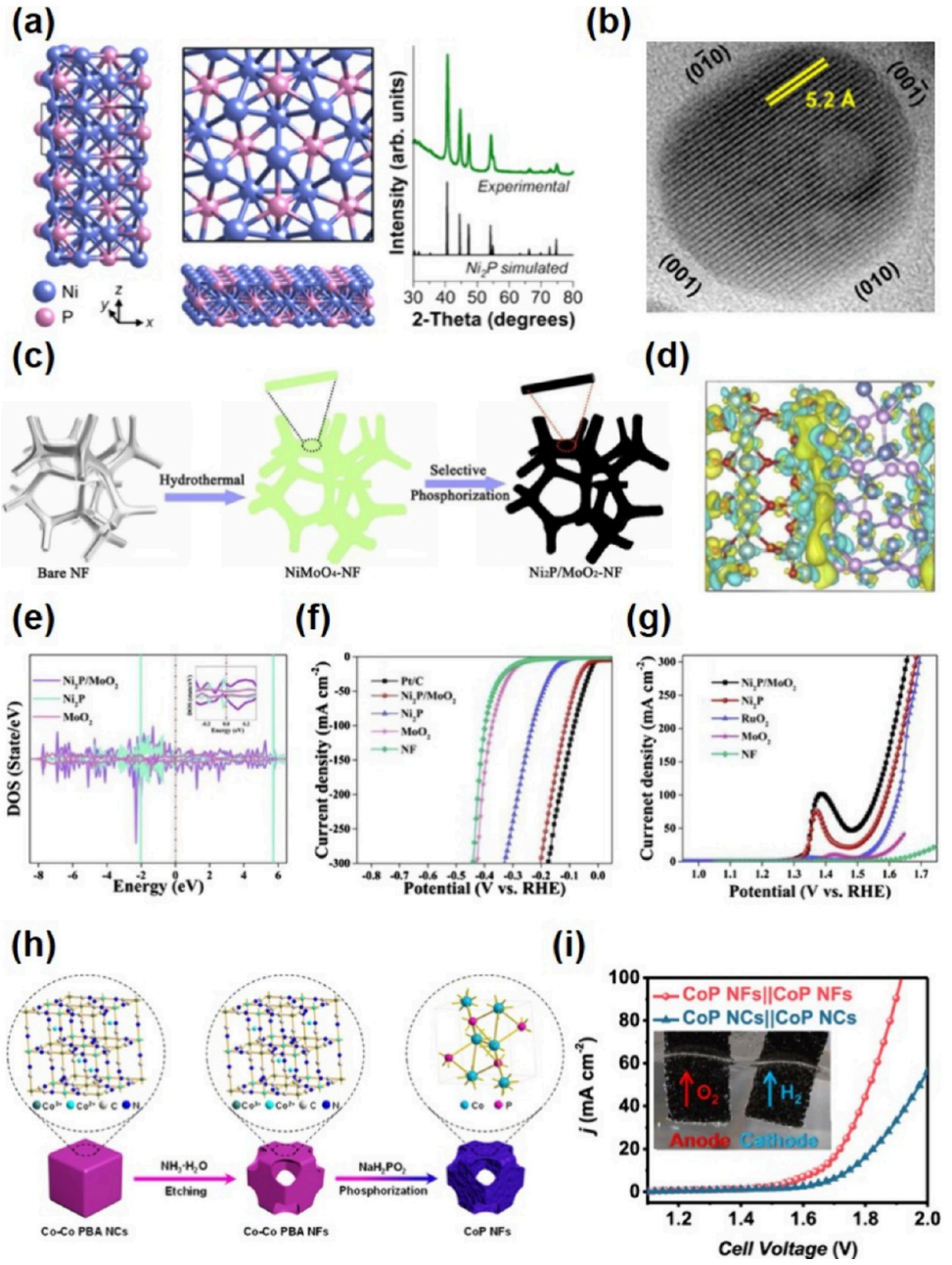

Figure 5. (a) Crystal structure of Ni_2P (001) surface (left), with experimental powder XRD pattern for the Ni_2P nanoparticles and the simulated pattern of Ni_2P shown for comparison (right). Reprinted with permission from ref 112. Copyright 2013, American Chemical Society. This article is an open access article distributed under the terms and conditions of the Creative Commons Attribution (CC-BY) license (https://creativecommons.org/licenses/by/4.0/). (b) HR-TEM image of representative Ni_2P nanoparticle, highlighting the exposed Ni_2P (001) facet and the 5.2 Å lattice fringes that correspond to the (010) planes. Reprinted with permission from ref 112. Copyright 2013, American Chemical Society. This article is an open access article distributed under the terms and conditions of the Creative Commons Attribution (CC-BY) license (https://creativecommons.org/licenses/by/4.0/). (c) Schematic illustration of the synthesis of Ni_2P/MoO_2/NF HNRs (heterostructure nanorods arrays). Reprinted with permission from ref 116. Copyright 2020, Elsevier. (d) The charge density difference in the heterostructures of Ni_2P/MoO_2. The yellow and blue isosurfaces represent charge accumulation and depletion in the space, respectively. And the isosurfaces level is 0.018 au. The red, green, pink, and light blue spheres represent O, Mo, P, and Ni atoms, respectively. Reprinted with permission from ref 116. Copyright 2020, Elsevier. (e) Calculated DOS for Ni_2P/MoO_2, Ni_2P, and MoO_2. The Fermi Level is set at 0 eV. Reprinted with permission from ref 116. Copyright 2020, Elsevier. (f) The polarization curves of HER on bare NF, MoO_2/NF, Ni_2P/NF, Pt/C/NF, and Ni_2P/MoO_2/NF HNRs in 1 M KOH. Reprinted with permission from ref 116. Copyright 2020, Elsevier. (g) The polarization curves of OER on bare NF, MoO_2/NF, Ni_2P/NF, RuO_2/NF, and Ni_2P/MoO_2/NF HNRs in 1 M KOH. Reprinted with permission from ref 116. Copyright 2020, Elsevier. (h) Synthesis of the CoP NFs (nanoframes). Reprinted with permission from ref 117. Copyright 2020, American Chemical Society. This article is an open access article distributed under the terms and conditions of the Creative Commons Attribution (CC-BY) license (https://creativecommons.org/licenses/by/4.0/). (i) LSV curves for CoP NFs||CoP NFs and CoP NCs (nanocubes) ||CoP NCs electrolyzers in 1 M KOH. Reprinted with permission from ref 117. Copyright 2020, American Chemical Society. This article is an open access article distributed under the terms and conditions of the Creative Commons Attribution (CC-BY) license (https://creativecommons.org/licenses/by/4.0/).

https://doi.org/10.1021/acsmaterialslett.4c00659
ACS Materials Lett. 2024, 6, 3133−3160

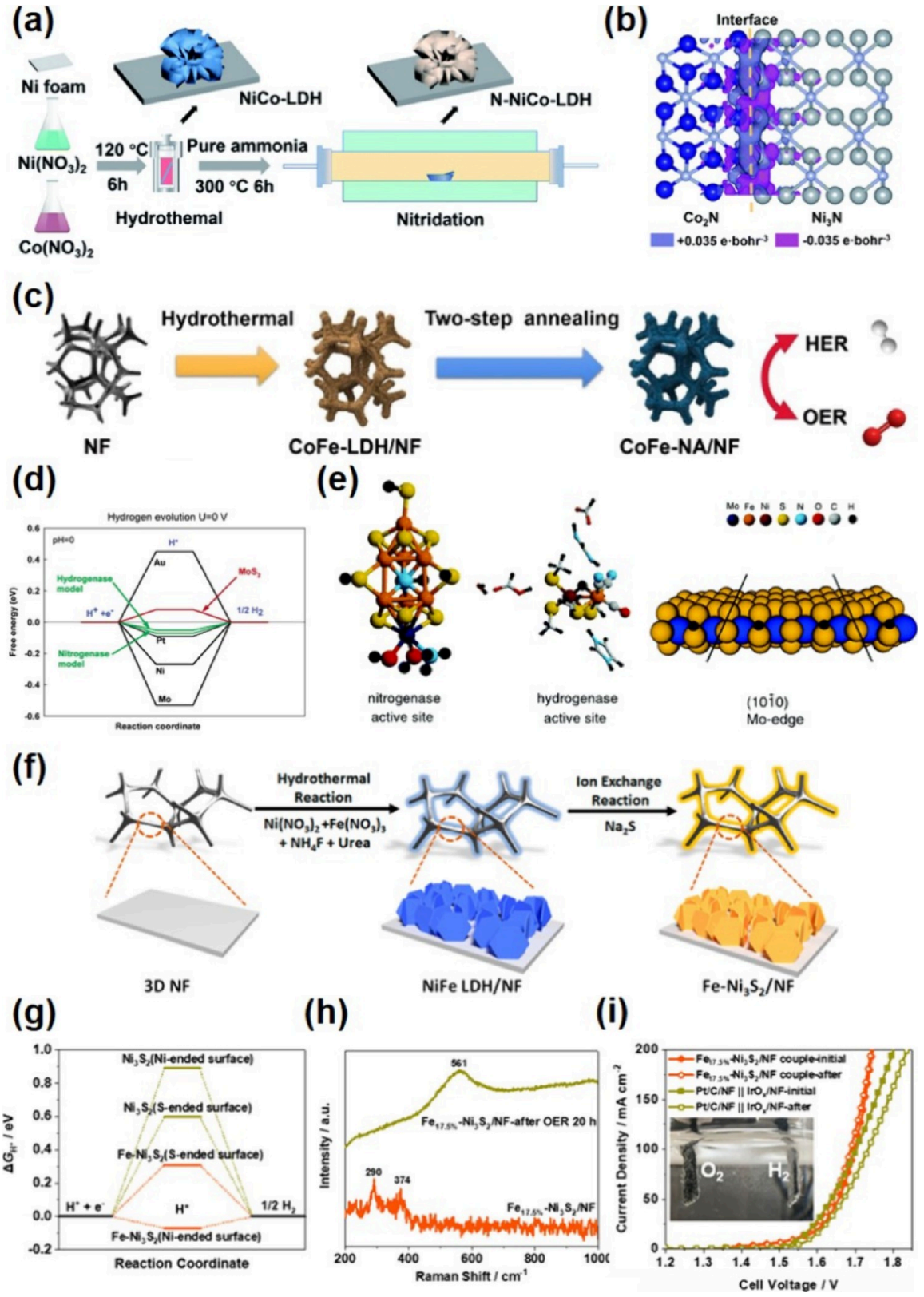

Figure 6. (a) Schematic illustration for the synthesis N-NiCo-LDH. Reprinted with permission from ref 121. Copyright 2021, The Royal Society of Chemistry. (b) Distribution of charge density differences at the Ni_3N/Co_2N interface in N-NiCo-LDH, where the blue and purple colors represent the accumulation and depletion of the electronics, respectively ($|\Delta\rho|$= 0.035 e $bohr^{-3}$). Reprinted with permission from ref 121. Copyright 2021, The Royal Society of Chemistry. (c) Schematic representation for the synthesis of CoFe-NA/NF electrodes. Reprinted with permission from ref 122. Copyright 2022, Elsevier. (d) Calculated free energy diagram for hydrogen evolution at a potential U = 0 relative to the standard hydrogen electrode at pH = 0. The free energy of $H^+ + e^-$ is by definition the same as that of $^1/_2$ H_2 at standard conditions. The free energy of H atoms bound to different catalysts is then found by calculating the free energy with respect to molecular hydrogen including zero-point energies and entropy terms. Reprinted with permission from ref 131. Copyright 2005, American Chemical

https://doi.org/10.1021/acsmaterialslett.4c00659
ACS Materials Lett. 2024, 6, 3133−3160

Figure 6. continued

Society. (e) Nitrogenase FeMo cofactor (FeMoco) with three hydrogen atoms bound at the equatorial μ_2S sulfur atoms (Left). Hydrogenase active site with one hydrogen atom bound (Middle). MoS_2 slab with sulfur monomers present at the Mo edge (Right). The coverage is 50%, i.e., hydrogen is bound at every second sulfur atom. The lines mark the dimension of the unit cell in the *x*-direction. Reprinted with permission from ref 131. Copyright 2005, American Chemical Society. (f) Schematic illustration of the fabrication of Fe−Ni_3S_2/NF. Reprinted with permission from ref 132. Copyright 2018, American Chemical Society. (g) Calculated free energy diagram of HER over the $(\bar{2}10)$ plane of Ni_3S_2 and Fe−Ni_3S_2. Reprinted with permission from ref 132. Copyright 2018, American Chemical Society. (h) Raman spectra of $Fe_{17.5\%}$-Ni_3S_2/NF before and after oxygen evolution for 20 h. Reprinted with permission from ref 132. Copyright 2018, American Chemical Society. (i) *iR*-corrected polarization curves of $Fe_{17.5\%}$-Ni_3S_2/NF‖$Fe_{17.5\%}$-Ni_3S_2/NF and Pt/C/NF‖IrO_x/NF water electrolyzers in 1 M KOH at 5 mV s^{-1}. The inset shows H_2 and O_2 bubbles evolving from $Fe_{17.5\%}$-Ni_3S_2/NF electrodes. Reprinted with permission from ref 132. Copyright 2018, American Chemical Society.

same time, Schaak, Lewis, and their colleagues reported the synthesis of catalytically active Ni_2P hollow nanoparticles, confirming the high density of the Ni_2P (001) surface as predicted by theory (Figure 5**a, b**).[112] Driven by these successes, the field of TMPs for water-splitting continues to flourish, as evidenced by the growing number of research publications.

That is, these reports highlight the promise of transition metal phosphides (TMPs) as quasi-platinum catalysts for water-splitting. Their combination of electrical/chemical stability, optimal conductivity, robust mechanical strength, and abundant unsaturated surface atoms renders them highly compelling.[113,114] One notable feature is the role of negatively charged phosphorus (P) atoms, which serve as effective proton traps and dissociation, boosting HER activity. Additionally, when TMPs are subjected to anodic potential, an amorphous transition metal oxyhydroxide shell is formed on the TMPs, which functions as an active shell for OER. This intrinsic bifunctionality positions TMPs as ideal candidates for efficient water-splitting.[70,115] Recent demonstrations have provided further insight into this potential. Yang et al. reported on the synthesis of Ni_2P/MoO_2 heterostructure nanorods using a selective phosphorization strategy (Figure 5c).[116] They also conducted the analyses on the work function, differential charge density, and density of states (DOS) of Ni_2P/MoO_2 to understand the effect of P atoms and electron structure change. These investigations revealed that the work function of Ni_2P (111) and MoO_2 (011) were estimated to be approximately 5.01 and 8.56 eV, respectively. These results indicated a reinforced dipole polarization at the interface between Ni_2P and MoO_2, resulting in the enhanced charge concentration and the increased electrocatalytic performance (Figure 5d). Furthermore, the DOS near the Fermi level for Ni_2P/MoO_2 was significantly higher than those of Ni_2P and MoO_2, suggesting the enhancements in electronic conductivity and electron transfer capacity. These structures exhibited remarkably low overpotentials for both HER (34 mV at 10 mA cm^{-2}) and OER (270 mV at 50 mA cm^{-2}), demonstrating their impressive bifunctional capabilities (Figure 5**e-g**). To further support this point, Ji et al. designed and synthesized CoP nanoframes using a multistep approach.[117] The resulting hollow structures, with highly dispersed and active sites, delivered superior bifunctional activity, achieving an overall water-splitting cell voltage of 1.65 V at 10 mA cm^{-2} (Figure 5**h, i**). As a result, the exceptional properties of TMPs, with their demonstrated bifunctionality in advanced nanostructures, position them as highly promising electrocatalysts for bifunctional AWS electrodes.

In addition to transition metal phosphides, transition metal nitrides (TMNs) with nitrogen (N) atoms in place of phosphorus (P) offer another promising avenue for electrocatalysis in water-splitting. The incorporation of N enhances catalytic activity in several ways: first, by increasing metallic conductivity for efficient electron transfer; second, by providing additional active sites for reaction; and third, by increasing corrosion resistance for long-term stability.[118−120] These benefits stem from the electronegativity of the N atoms. Within the metal lattice, N increases metal spacing and weakens interatomic forces. This, in turn, allows N to control the *d*-electron density and narrow the *d*-band of TMNs. This fine-tuned electronic tuning then regulates the adsorption and desorption energies of key intermediates in water-splitting reactions, optimizing catalytic performance. In particular, bimetallic TMNs, which utilize the synergistic action of two metals, have emerged as more effective bifunctional electrocatalysts than single-metal nitrides for both HER and OER, demonstrating exceptional advantages in AWS: abundant active sites for efficient reactions and robust chemical/structural stability for sustained performance.

Synthesis of TMNs typically involves topochemical processes, utilizing metal oxides and nitrogen sources such as N_2, NH_3, urea, or organic compounds. A representative example comes from Wen et al., who designed a Ni_3N/Co_2N bimetallic heterojunction within NiCo-LDH via calcination in pure ammonia (Figure 6a).[121] This unique structure reinforced electron interactions, optimized intermediate adsorption, and facilitated water-splitting (Figure 6b). The resulting Ni_3N/Co_2N on Ni foam achieved remarkable performance: low HER overpotential of 35 mV at 10 mA cm^{-2} with a Tafel slope of 34 mV dec^{-1}, and a cell voltage of 1.55 V at 10 mA cm^{-2} without *iR* compensation. Another impressive demonstration came from Chen et al., who fabricated CoFe-N alloy nanosheets on nickel foam using a hydrothermal and two-step calcination approach with urea and NH_3 (Figure 6c).[122] These nanosheets exhibited low hydrogen and water adsorption energies, resulting in high HER activity (overpotential of 73 mV at 10 mA cm^{-2}). Interestingly, the surface reconstruction from CoFe-N to metal oxyhydroxides significantly boosted electrostatic adsorption of OH^- ions, leading to excellent OER performance (overpotential of 250 mV at 10 mA cm^{-2}).

Beyond TMPs and TMNs, transition metal chalcogenides (TMCs) - which include elements such as sulfur (S), selenium (Se), tellurium (Te), and others - have also received significant attention in water-splitting applications.[123,124] Their appeal lies in a unique confluence of advantages: affordability, abundant defect sites, tunable electronic structures, diverse morphologies, and impressive electrocatalytic properties. Within this class, transition metal sulfides (TMSs) such as MoS_2,[125] WS_2,[126] CoS_2,[127] CuS,[128] FeS_2,[129] and NiS_2[130] are particularly

https://doi.org/10.1021/acsmaterialslett.4c00659
ACS Materials Lett. 2024, 6, 3133−3160

Table 1. Electrochemical Performances Comparison of Transition Metal-Based Water-Splitting Electrodes in AWS

Water-Splitting Electrode	Fabrication Method	HER Overpotential (mV)	OER Overpotential (mV)	Overall Cell Voltage (V)	Operational Stability	ref
Ni-FeO_x/$FeNi_3$/Ni foam	Combution process, Calcination	71 @50 mA cm^{-2}	269 @50 mA cm^{-2}	1.58 @50 mA cm^{-2}	100 h @30 mA cm^{-2}	161
		272 @1000 mA cm^{-2}	405 @1000 mA cm^{-2}	1.80 @500 mA cm^{-2}		
Cu/Cu_2O/NiO @NiCu foam	Hydrothermal method, Calcanation, Electroreduction	79 @10 mA cm^{-2}	-	-	100 h @10 mA cm^{-2}	162
CoFeZr oxides/Ni foam	Solvothermal method	104 @10 mA cm^{-2}	264 @20 mA cm^{-2}	1.63 @10 mA cm^{-2}	12 h @10 mA cm^{-2}	101
			282 @50 mA cm^{-2}			
HER: NiMo M/O @glassy carbon	Hydrothermal method, Calcination	16 @10 mA cm^{-2}	221 @10 mA cm^{-2}	1.53 @10 mA cm^{-2}	-	163
OER: NiFeMo M/O @glassy carbon		50 @50 mA cm^{-2}				
MoO_3/Ni-NiO @Carbon cloth	Electrodeposition	62 @10 mA cm^{-2}	347 @100 mA cm^{-2}	1.55 @10 mA cm^{-2}	20 h @10 mA cm^{-2}	102
Ce @NiCo-LDH/Ni foam	Hydrothermal method	134 @50 mA cm^{-2}	250 @50 mA cm^{-2}	1.68 @10 mA cm^{-2}	35 h @10 mA cm^{-2}	164
NiFeV LDH/Ni foam	Hydrothermal method	-	192 @10 mA cm^{-2}	-	18 h @187 mA cm^{-2}	109
$Ni_{0.83}Fe_{0.17}(OH)_2$/glassy carbon	Solvothermal method, Cation-exchange reaction	-	245 @10 mA cm^{-2}	-	10 h @10 mA cm^{-2}	108
CoFe-LDH@NiSe/Ni foam	Hydrothermal method, Selenization, Electrodeposition	38 @10 mA cm^{-2}	127 @10 mA cm^{-2}	1.51 @10 mA cm^{-2}	120 h @10 mA cm^{-2}	107
P−V−NiFe LDH NSA[a]/ Ni foam	Hydrothermal method, Plasma reduction	19 @10 mA cm^{-2}	295 @100 mA cm^{-2}	1.43 @10 mA cm^{-2}	1000 h @40 mA cm^{-2}	165
HER: H-NiFe LDH/Ni foam	Hydrothermal method, Chemical aging method	59 @10 mA cm^{-2}	184 @10 mA cm^{-2}	1.48 @10 mA cm^{-2}	100 h @10 mA cm^{-2}	166
OER: O-NiFe LDH/Ni foam						
CoP nanoframe/glassy carbon	Chemical etching, Phosphorization	136 @10 mA cm^{-2}	323 @10 mA cm^{-2}	1.65 @10 mA cm^{-2}	30 h @15 mA cm^{-2}	117
Co−Ni_2P/Carbon fiber cloth	Hydrothermal method, Calcination, Phosphorization	31 @10 mA cm^{-2}	-	-	20 h @20 mA cm^{-2}	167
Ni_2P/MoO_2/Ni foam	Hydrothermal method,Phosphorization	34 @10 mA cm^{-2}	-	-	-	116
Ni−Mn−FeP/NiFe Foam	Chemical etching, Phosphorization	103 @10 mA cm^{-2}	185 @10 mA cm^{-2}	1.48 @10 mA cm^{-2}	360 h @500 mA cm^{-2}	168
		177 @100 mA cm^{-2}	205 @100 mA cm^{-2}			
CoFe-NA[b]/Ni foam	Hydrothermal method, Calcination, Nitridation	73 @10 mA cm^{-2}	250 @10 mA cm^{-2}	1.564 @10 mA cm^{-2}	50 h @10 mA cm^{-2}	122
Ni_3FeN/r-GO/aerogel	Ion-exchange process, nitrogenization	94 @10 mA cm^{-2}	270 @10 mA cm^{-2}	1.60 @10 mA cm^{-2}	100 h @10 mA cm^{-2}	169
Ni_3N/Co_2N-LDH/Ni foam	Hydrothermal method, Nitridation	35 @10 mA cm^{-2}	250 @10 mA cm^{-2}	1.55 @10 mA cm^{-2}	24 h @10 mA cm^{-2}	121
$Fe_xNi_{3-x}S_2$/Ni foam	Chemical etching	72 @10 mA cm^{-2}	252 @100 mA cm^{-2}	1.51 @10 mA cm^{-2}	64 h @500 mA cm^{-2}	170
Fe−Ni_3S_2/Ni foam	Hydrothermal method, Ion exchange reation	47 @10 mA cm^{-2}	214 @10 mA cm^{-2}	1.54 @10 mA cm^{-2}	10 h @20 mA cm^{-2}	132
		142 @20 mA cm^{-2}	222 @20 mA cm^{-2}			
		232 @100 mA cm^{-2}	249 @100 mA cm^{-2}			
N−Ni_3S_2/Ni foam	Selenizaition, Nitridation	110 @10 mA cm^{-2}	330 @100 mA cm^{-2}	1.48 @10 mA cm^{-2}	8 h @20 mA cm^{-2}	171
N-NiS_2/glassy carbon	Selenizaition, Nitridation	-	295 @20 mA cm^{-2}	-	24 h @10 mA cm^{-2}	172
NiP_2/$NiSe_2$/Carbon fiber cloth	Phosphoselenization	89 @10 mA cm^{-2}	250 @10 mA cm^{-2}	1.56 @10 mA cm^{-2}	30 h @10 mA cm^{-2}	173
		160 @100 mA cm^{-2}	329 @100 mA cm^{-2}			
CPF-Fe/Ni/Carbon cloth	Solvothermal method	42 @10 mA cm^{-2}	194 @10 mA cm^{-2}	1.57 @10 mA cm^{-2}	200 h @10 mA cm^{-2}	174
Ni_2P/V-Pi/Carbon cloth	Hydrothermal method, Oxidation, Phosphorization	80.8 @10 mA cm^{-2}	245 @10 mA cm^{-2}	1.44 @10 mA cm^{-2}	20 h @10 mA cm^{-2}	175
NiFe LDH-NiSE/Ni foam	Hydrothermal method	276 @100 mA cm^{-2}	240 @100 mA cm^{-2}	1.53 @10 mA cm^{-2}	75 h @114 mA cm^{-2}	176

https://doi.org/10.1021/acsmaterialslett.4c00659
ACS Materials Lett. 2024, 6, 3133−3160

Table 1. continued

Water-Splitting Electrode	Fabrication Method	HER Overpotential (mV)	OER Overpotential (mV)	Overall Cell Voltage (V)	Operational Stability	ref
$Ni_3Fe_{1-x}Cr_x$/Carbon cloth	Carbothermal shock method	128 @10 mA cm^{-2}	239 @10 mA cm^{-2}	1.59 @10 mA cm^{-2}	20 h @10 mA cm^{-2}	177
Ni_6Mo_6C/$NiMoO_x$/Carbon cloth	Hydrothermal method, Carbothermal hydrogen reduction	29 @10 mA cm^{-2}	-	-	60 h @50 mA cm^{-2}	178
V-CoP@a-CeO_2/Carbon cloth	Phosphorization, Electrodeposition	68 @10 mA cm^{-2}	225 @10 mA cm^{-2}	1.56 @10 mA cm^{-2}	35 h @20 mA cm^{-2}	179
		140 @100 mA cm^{-2}	300 @20 mA cm^{-2}	1.71 @100 mA cm^{-2}		
			340 @100 mA cm^{-2}			
N-CoP/CeO_2/Carbon cloth	Hydrothermal method, Nitridation, Phosphorization	217 @100 mA cm^{-2}	215 @10 mA cm^{-2}	1.52 @10 mA cm^{-2}	504 h @400 mA cm^{-2}	180
		333 @200 mA cm^{-2}				
		538 @300 mA cm^{-2}				
$NiSe_2$/3DSNG[c]/Ni foam	Chemical vapor deposition, Hydrothermal method	117 @10 mA cm^{-2}	256 @100 mA cm^{-2}	1.59 @10 mA cm^{-2}	50 h @20 mA cm^{-2}	181
		247 @50 mA cm^{-2}				
		269 @100 mA cm^{-2}				
$NiSe_2$/Ni_3Se_4/Ni foam	Calcination, Selenization	145 @10 mA cm^{-2}	309 @100 mA cm^{-2}	1.56 @10 mA cm^{-2}	36 h @10 mA cm^{-2}	182
Sm@NiCu-LDH/Ni foam	Hydrothermal method	192 @50 mA cm^{-2}	347 @50 mA cm^{-2}	1.629 @10 mA cm^{-2}	36 h @10 mA cm^{-2}	183
Ni_xS_y@MnO_xH_y/Ni foam	Hydrothermal method, Electrodeposition	179 @10 mA cm^{-2}	326 @100 mA cm^{-2}	1.53 @10 mA cm^{-2}	100 h @100 mA cm^{-2}	184
			347 @300 mA cm^{-2}			
		270 @100 mA cm^{-2}	356 @500 mA cm^{-2}			
Co_2P–Ni_3S_2/Ni foam	Hydrothermal method, Phosphorization	110 @100 mA cm^{-2}	331.7 @100 mA cm^{-2}	1.54 @10 mA cm^{-2}	24 h @100 mA cm^{-2}	185
		164 @500 mA cm^{-2}	358.3 @500 mA cm^{-2}			
O-CoP/Ni foam	Hydrothermal method, Calcination, Phosphorization	124 @100 mA cm^{-2}	312 @400 mA cm^{-2}	1.56 @20 mA cm^{-2}	24 h @20 mA cm^{-2}	186
		174.9 @400 mA cm^{-2}				
Cu_3N/Ni foam	Nitridation, Electrodeposition	118 @10 mA cm^{-2}	286 @10 mA cm^{-2}	1.6 @10 mA cm^{-2}	240 h @10 mA cm^{-2}	187

[a]NSA: nanosheet array. [b]NS: nitride/alloy nanosheet. [c]DSNG: S,N codoped graphene foam

promising. Their high catalytic activity makes them attractive in various scientific fields, from electronics to electrocatalysis. In addition, compared to other TMOs, the TMSs often exhibit superior electrical conductivity due to their narrower band gaps, which gives them semiconductor-like behavior.

Initially, transition metal sulfides (TMS), especially layered MoS_2, dominated research as promising HER electrocatalysts. In 2005, the Nørskov group used DFT calculations to shed light on the potential of MoS_2.[131] They showed that the $(10\bar{1}0)$ Mo-edge structure of MoS_2 bears striking similarities to nitrogenase, a natural hydrogen-producing enzyme. In addition, they found that the MoS_2 edge serves as an active HER site with a Gibbs free energy of hydrogen adsorption (ΔG_{H^*}) close to that of platinum, the benchmark catalyst. This discovery sparked numerous research efforts to experimentally and theoretically locate the active sites of MoS_2 for HER (Figure 6**d**, **e**).

Interestingly, while some TMSs show susceptibility to oxidation, transforming into corresponding oxides/(oxy)-hydroxides, this does not diminish their promise for OER. In fact, these postoxidized catalysts often outperform directly synthesized single metal oxides/hydroxides. A recent study by Zhang et al. illustrated this by presenting a free-standing electrocatalyst consisting of vertically oriented Fe-doped Ni_3S_2 nanosheet arrays grown on Ni foam (Figure 6f).[132] This innovative structure exhibited remarkable activity and durability for both HER and OER. The Fe-doping imparted metallic behavior to Ni_3S_2, which resulted in exceptional electronic conductivity and optimized water and H adsorption on the catalyst surface, thereby enhancing the intrinsic HER activity of the active sites (Figure 6g). In addition, during the OER process, the near-surface sulfide was transformed into Ni–Fe(oxy)hydroxide, a more active material than single-component Ni(oxy)hydroxide (Figure 6h). This conversion further improved the overall performance. When integrated into a water-splitting electrolyzer, the Fe-doped Ni_3S_2/Ni foam catalyst achieved a remarkable cell voltage of 1.54 V at a current density of 10 mA cm^{-2} (Figure 6i).

Although these various transition metal-based catalysts, including oxides, hydroxides, phosphides, nitrides, and sulfides, offer exciting possibilities for efficient water-splitting due to their impressive oxidation–reduction capabilities, their corre-

https://doi.org/10.1021/acsmaterialslett.4c00659
ACS Materials Lett. 2024, 6, 3133–3160

sponding electrocatalytic performance has not yet reached substantial practical value for large-scale hydrogen energy production. Specifically, Table 1 shows the electrocatalytic performance of some transition metal-based catalysts reported in recent years. Despite the impressive water-splitting performance metrics such as low overpotentials and Tafel slopes, many of these electrocatalysts operate at only low current densities (<500 mA cm^{-2}) and suffer from inadequate stability (<500 h). These limitations render them unsuitable for the commercially available AWS systems. Although these highly efficient electrocatalysts are crucial, the successful development of AWS electrodes with low overpotentials and enduring stability at high current densities relies not solely on these catalysts. As mentioned earlier, it requires favorable interfacial interactions between host electrode and electrocatalysts as well as between adjacent electrocatalysts. Moreover, integrating highly conductive host electrodes with a substantial specific surface area is essential. This integration allows the combination of significant amounts of electrocatalysts, including highly efficient ones, to form effective AWS electrodes.

To significantly enhance the performance of the overall water-splitting electrode, it is imperative to carefully address both the structural and interfacial aspects of the HER and OER electrodes, as well as the intrinsic electrochemical properties of the electrocatalysts. Of particular note is the observation that at high current densities, most electrocatalysts experience reduced activity and active attenuation due to increased electron consumption.[45,46,133] This results in an insufficient supply of electrons from the host electrode to the active sites of the electrocatalysts. In addition, during the water-splitting reaction, the accumulation of substantial amounts of bubbles on the electrodes can block these active sites, potentially leading to the formation of inactive regions as well as the electrocatalyst delamination on the electrodes.[22,43,45] Thus, the shape, surface area, and interfacial properties of the host electrodes play a critical role in ensuring the secure attachment of the electrocatalysts, which directly affects the water-splitting efficiency and long-term stability of the electrodes. Furthermore, it is highly desirable that the host electrodes have a large surface area, resist electrochemical corrosion during the water-splitting reaction, and have a strong affinity for the electrocatalysts.

To significantly enhance the performance of the overall water-splitting electrode, it is imperative to carefully address both the structural and interfacial aspects of the HER and OER electrodes, as well as the intrinsic electrochemical properties of the electrocatalysts.

In the following sections, we describe recent advances in 3D porous structure-based AWS electrodes. Specifically, we not only explore the fabrication intricacies of the 3D host electrodes and electrocatalysts but also elucidate how the structural and interfacial design of the host electrode influence parameters such as charge transfer resistance, Tafel slopes, overpotentials, and operational stability of AWS electrodes.

Water-splitting researchers have used porous host electrode materials such as Ni foam and carbon cloth for AWS electrodes to take advantage of their large active surface area. In particular, Ni foam has emerged as a preferred choice due to its exceptional electrical conductivity, interconnected porous structure, relatively large specific surface area, and impressive corrosion resistance in AWS environments.[41,134] Similarly, carbon cloth has attracted attention for its favorable properties, including good electrical conductivity, chemical stability in alkaline media, lightweight, and desirable flexibility, making it a promising host electrode for water-splitting electrodes.[48,135] Based on these properties, numerous scientific research groups have developed various fabrication methods to produce the high-performance AWS electrodes using Ni foam and carbon cloth. Specifically, deposition techniques such as hydrothermal synthesis, electrodeposition, chemical etching, and more have been explored (Table 1). However, these substrates (i.e., Ni foam and carbon cloth) share a common drawback: their hydrophobic surfaces,[136,137] which have not taken into account the interfacial interaction between host electrode and electrocatalysts, impede the uniform deposition of electrocatalysts, thus hindering the enhancement of electrocatalytic activity within AWS systems.

As an alternative to improve the electrocatalytic performance and stability of AWS electrodes, some researchers have explored unique 3D-structured substrate materials, such as textiles and papers. These substrates offer several advantages, including lightweight, high mechanical flexibility, a large specific surface area and, hydrophilicity.[138−141] However, it should be noted that they are inherently insulating and face challenges in forming a conductive layer necessary for achieving the desired level of electrical conductivity. Several strategies have been suggested to address these challenges and impart electrical conductivity to these substrates. These methods include electroless deposition, hydrothermal synthesis, sputtering methods, drop casting, and more. Based on these approaches, the resulting conductive textile and/or paper-based water-splitting electrodes have shown promising electrocatalytic performances in the field of AWS (Table 2).

In particular, electroless plating process, also known as chemical reduction, has been extensively utilized in the fabrication of AWS electrodes, especially those based on 3D-structured host electrodes with complex shapes. For instance, in 2018, Bhattacharyya's group fabricated electrically conductive paper using Ni−P electroless plating process.[49] This process involves the reduction of metal ions from the aqueous solution with a reducing agent (e.g., NaH_2PO_2) and catalysts (e.g., Sn^0 and Pd^0) (Figure 7a). As a result, the thickness of Ni−P conductive layer was approximately 18 nm, reducing the sheet resistance of the paper-based host electrode to ∼4.2 Ω sq^{-1} from its initial insulating value for bare cellulose paper. Similarly, Hao et al. developed the paper-based host electrodes for bifunctional AWS electrode using a dip-coating and electroless plating process (Figure 7b).[142] The insulating paper substrate was activated by alternately dipping into $NiSO_4$ and $NaBH_4$ solutions. Then, the pretreated substrate was immersed in an aqueous electroless plating solution containing $NiSO_4$, NaH_2PO_2, Et_2NHBH_3, and Na_2SO_4 for 60 min at 10 °C to fabricate the Ni−P−B/paper electrode. The conductivity of the electrode was confirmed by series connecting the electrodes with a light emitting diode (LED) in a circuit. The illuminated LED indicated that the electrode had sufficient conductivity, and the sheet resistance of the electrode was

https://doi.org/10.1021/acsmaterialslett.4c00659
ACS Materials Lett. 2024, 6, 3133−3160

Table 2. Electrochemical Performances Comparison of 3D Structured-Textile and Paper-Based Water-Splitting Electrodes in AWS

Host Electrode Fabrication	Electrocatalysts	Deposition Method	HER Overpotential (mV)	OER Overpotential (mV)	Overall Cell Voltage (V)	Operational Stability	ref
LbL-assembled metal NPs	HER: Ni OER: NiFe LDH	Electrodeposition	12 @10 mA cm^{-2}	214 @50 mA cm^{-2}	1.39 @10 mA cm^{-2}	100 h @1000 mA cm^{-2}	146
Small molecular linker-based MWCNT assembly	HER: NiMo OER: NiFe	Electrodeposition	8 @10 mA cm^{-2}	189 @50 mA cm^{-2}	2.01 @3000 mA cm^{-2}	1000 h @3000 mA cm^{-2}	156
Carbonization/interfacial assemly	HER: Ni OER: NiFeCo	Electrodeposition	12 @10 mA cm^{-2}	186 @50 mA cm^{-2}	1.7 @2000 mA cm^{-2}	1640 h @2000 mA cm^{-2}	159
Electroless plating	HER: NiMo OER: NiFe	Electrodeposition	32 @10 mA cm^{-2}	240 @50 mA cm^{-2}	1.51 @10 mA cm^{-2}	200 h @10 mA cm^{-2}	49
Carbonization	Fe-NiSe	Calcination, Selenization	-	220 @10 mA cm^{-2}	-	20 h @10 mA cm^{-2}	188
Carbonization	Co	Calcination	74 @10 mA cm^{-2}	330 @10 mA cm^{-2}	1.40 @10 mA cm^{-2}	110 h @10 mA cm^{-2}	144
Electroless plating	NiFeP	Electroless plating	158 @10 mA cm^{-2}	282 @10 mA cm^{-2}	1.814 @100 mA cm^{-2}	30 h @100 mA cm^{-2}	189
Electroless plating	CoMo	Electrodeposition	46 @10 mA cm^{-2}	250 @10 mA cm^{-2}	1.55 @10 mA cm^{-2}	200 h @200 mA cm^{-2}	190
Carbonization	Co_9S_8@Co−N	Calcination	152 @10 mA cm^{-2}	373 @10 mA cm^{-2}	1.61 @10 mA cm^{-2}	70 h @10 mA cm^{-2}	191
Carbonization	Ni/N/C	Calcination	190 @10 mA cm^{-2}	390 @10 mA cm^{-2}	-	10 h @15 mA cm^{-2}	192
Electrospinning, Carbonization	Ni/Mo_2C	Calcination	143 @10 mA cm^{-2}	288 @10 mA cm^{-2}	1.64 @10 mA cm^{-2}	100 h @10 mA cm^{-2}	193
Electroless plating	NiP	Electroless plating	159 @10 mA cm^{-2} 281 @100 mA cm^{-2}	-	-	-	194
Carbonization	Co_3S_4	Hydrothermal method	100 @10 mA cm^{-2}	240 @10 mA cm^{-2}	1.57 @10 mA cm^{-2}	80 h @10 mA cm^{-2}	195
Electroless plating	Ag/Ni	Galvanic Replacement Reaction	216 @10 mA cm^{-2}	-	-	20 h @8 mA cm^{-2}	196
Carbonization	Fe_3O_4/NiS	Calcination	-	310 @10 mA cm^{-2}	-	25 h @10 mA cm^{-2}	197
Carbonization, Activation	CuS/ZnO	Dip coating, Vacuum Thermal Evaporation Technology	-	337 @10 mA cm^{-2}	-	-	158
Electrospinning, Carbonization	MO_2C-CoO	Calcination	115 @10 mA cm^{-2}	222 @10 mA cm^{-2}	1.56 @10 mA cm^{-2}	30 h @45 mA cm^{-2}	145
Electroless plating	Ni−P−B	Electroless plating	76 @10 mA cm^{-2}	263 @10 mA cm^{-2}	1.661 @50 mA cm^{-2}	240 h @1000 mA cm^{-2}	142
Electroless plating	Co−Ni−P	Electroless plating	125 @10 mA cm^{-2}	320 @10 mA cm^{-2}	1.66 @10 mA cm^{-2}	24 h @10 mA cm^{-2}	198
Sputtering	$Co(OH)_2$@Ni	Electrodeposition	96 @10 mA cm^{-2}	300 @10 mA cm^{-2}	1.64 @10 mA cm^{-2}	10 h @10 mA cm^{-2}	199
Electroless plating	CoP	Electrodeposition	63 @10 mA cm^{-2}	-	-	15 h @10 mA cm^{-2}	200

measured to be approximately 0.42 Ω sq^{-1} (Figure 7c). Although electroless deposition effectively converts insulating substrates into conductive host electrodes, as previously noted, it often causes metal clusters to agglomerate and block the pore structures within 3D-structured substrate materials. This occurs due to the rapid and continuous reduction of metal ions. Additionally, this process usually requires the use of reducing agents and noble metal catalysts, particularly Pd, to aid in the nucleation and growth of metal ions.[50,51]

Another promising approach for fabricating textile and/or paper-based electrodes involves the carbonization process with transition metal-based catalyst precursors. During carbonization in an inert environment, the well-aligned linear sp^3 and/or sp^2 hybridized carbon structures (e.g., silk, polyester, nylon, poly(vinylpyrrolidone) (PVP), poly(acrylonitrile) (PAN)) and poly(saccharide) structures (e.g., cotton, paper, cellulose fiber) can be converted into polyaromatic structures that serve as electron pathways.[143] For example, Jiang et al. demonstrated the use of cobalt-supported cotton fiber electrodes for the overall water-splitting in alkaline media.[144] In their study, the cotton fiber was immersed in a 5 wt % $CoCl_2$ aqueous solution, and then subsequently carbonized at 800 °C. These carbonized cotton fibers served as conductive host electrodes, while Co^{2+} ions from the precursor solution were converted into metallic Co particles on the surface of the carbonized cotton fiber. This in situ transformation was confirmed through various analyses including X-ray photoelectron spectroscopy (XPS), X-ray adsorption near edge structure (XANES), and extended X-ray absorption fine structure (EXAFS) analysis. As a result, the Co-decorated carbonized cotton fiber electrodes exhibited good water-splitting performances, achieving low overpotentials of 74 mV for HER and 330 mV for OER at a current density of 10 mA cm^{-2}. These electrodes also exhibited relatively good

https://doi.org/10.1021/acsmaterialslett.4c00659
ACS Materials Lett. 2024, 6, 3133−3160

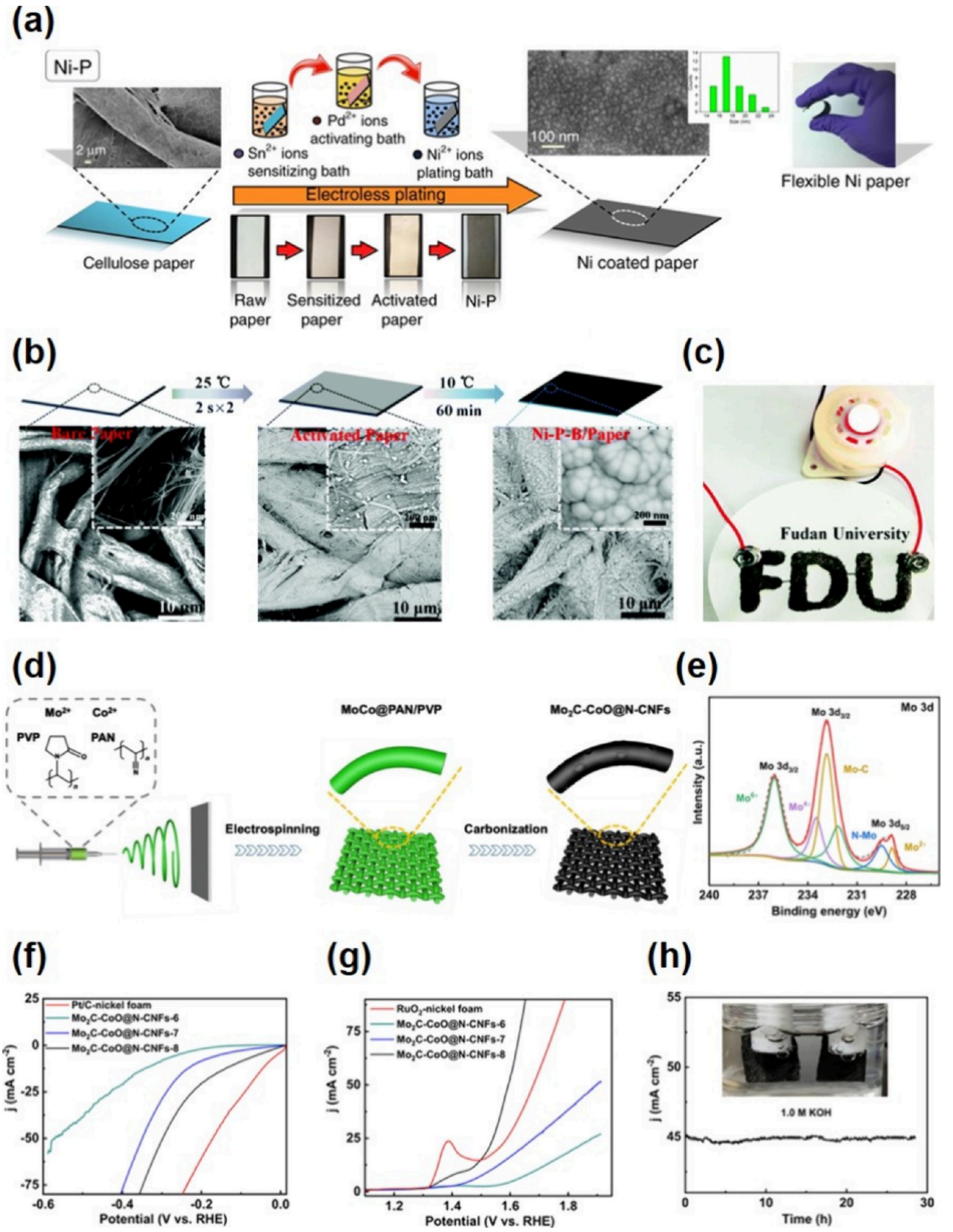

Figure 7. (a) Schematic illustration of the fabrication process for Ni−P electrodes. Reprinted with permission from ref 49. Copyright 2018, Springer Nature. This article is an open access article distributed under the terms and conditions of the Creative Commons Attribution (CC-BY) license (https://creativecommons.org/licenses/by/4.0/). (b) Schematic synthetic process for the Ni−P−B/paper electrode. And SEM images of bare paper (left), activated paper (middle), and Ni−P−B/paper electrode (right). Reproduced with permission from ref 142. Copyright 2020, The Royal Society of Chemistry. (c) Photograph of the conductive Ni−P−B/paper electrode with a sign of "FDU" (Fudan

https://doi.org/10.1021/acsmaterialslett.4c00659
ACS Materials Lett. 2024, 6, 3133−3160

Figure 7. continued

University). Reproduced with permission from ref 142. Copyright 2020, The Royal Society of Chemistry. (d) Schematic illustration for the preparation process of the self-standing Mo_2C-CoO@N-CNFs film. Reprinted with permission from ref 145. Copyright 2023, Elsevier. (e) High resolution XPS spectra for Mo 3d for the Mo_2C-CoO@N-CNFs electrode. Reprinted with permission from ref 145. Copyright 2023, Elsevier. (f) HER polarization curves of Pt/C-nickel foam, Mo_2C-CoO@N-CNFs-6 (carbonized at 600 °C), Mo_2C-CoO@N-CNFs-7 (carbonized at 700 °C), and Mo_2C-CoO@N-CNFs-8 (carbonized at 800 °C). Reprinted with permission from ref 145. Copyright 2023, Elsevier. (g) OER polarization curves of RuO_2-nickel foam, Mo_2C-CoO@N-CNFs-6, Mo_2C-CoO@N-CNFs-7, and Mo_2C-CoO@N-CNFs-8. Reprinted with permission from ref 145. Copyright 2023, Elsevier. (h) Time-dependent current density curve of the Mo_2C-CoO@N-CNFs||Mo_2C-CoO@N-CNFs and Pt/C-nickel foam||RuO_2-nickel foam cell in 1 M KOH. Reprinted with permission from ref 145. Copyright 2023, Elsevier.

operational stability, maintaining activity for 110 h at the same current density in 1 M KOH. In a related development, recent research by Gong et al. introduced PAN/PVP-based 3D-structured electrodes decorated with Mo_2C and CoO (Figure 7d).[145] These electrodes were prepared through a series of processes including electrospinning, oxidation, and carbonization. Similar to the previous study mentioned, PAN and PVP were dissolved in dimethylformamide (DMF) with $MoCl_5$ and $Co(CH_3COOH)_2$. The resulting spinning precursor solution was collected on Al foil by electrospinning process, followed by carbonization at high temperatures ranging from 600 to 900 °C. In this case, the XPS analysis revealed characteristic peaks in the Mo 3d spectrum at 228.8 and 232.8 eV, indicating the presence of Mo(II) in Mo_2C (Figure 7e). Additionally, the presence of the Mo−N bond at 229.5 eV suggested the interaction between Mo_2C and PAN/PVP-based host electrode. Furthermore, the Co 2p spectrum exhibited two main spin orbital peaks at 781.6 and 796.9 eV, indicating the Co(II) oxide, which correlated with the O 1s spectrum. These optimized integrated electrodes demonstrated high electrocatalytic activities for both HER and OER, with overpotentials of 115 mV for HER and 200 mV for OER at a current density of 10 mA cm^{-2} in 1 M KOH (Figure 7**f, g**). However, these electrodes exhibited insufficient operational stability, sustaining activity for only 30 h at a low current density of 45 mA cm^{-2} (Figure 7h).

While several studies have effectively converted the insulating textile or paper-based substrates into the conductive host electrodes, the critical challenges arise due to the lack of strong interfacial adhesion. Weak bonds between the conductive layer and the electrocatalysts as well as between the substrate surface and the conductive layer can lead to significant chemical and mechanical damage. This may encompass the detachment of electrocatalysts from the host electrode and the dissolution of electrocatalysts in alkaline media during electrochemical water-splitting reactions, particularly at high current densities. Therefore, it is essential to carefully consider all the components, including substrate materials, conductive layer, organic molecules, and electrocatalysts, to achieve high performance and outstanding operational stability in AWS.

Highly porous natural cotton textiles and paper materials, which are composed of numerous cellulose fibrils, typically exhibit abundant hydroxyl groups, resulting in excellent surface wettability in electrolyte solutions. As already mentioned in previous section, taking advantage of this hydrophilic surface property, various electrocatalytic metal ions can be directly deposited on 3D-structured textiles and papers for AWS electrodes. This approach can result in enhanced water-splitting performance compared to 2D-structured or conventional Ni foam-based AWS electrodes. Despite the success of these chemical reduction methods in creating AWS textile electrodes with intricate fibril structures, challenges remain in achieving highly uniform coatings and structures. This difficulty stems from the inadequate control of the interfacial interactions between the textile substrate and the introduced conductive, catalytic components. Consequently, these limitations can affect the overall conductivity and catalytic activity in water-splitting electrochemical reactions.

As an alternative to chemical reduction approaches, Ko et al. recently introduced electrocatalytic cotton textile electrodes for AWS using a layer-by-layer (LbL) assembly induced transition metal electroplating method (Figure 8a).[146] Generally, it is well-known that a LbL assembly is potentially the most versatile and well-established method, enabling tailored functionalities, thicknesses and chemical compositions through complementary interactions (i.e., electrostatic, hydrogen-bonding, or covalent-bonding interactions) between adjacent components.[147−155] Using this LbL assembly, the cotton textiles, characterized by OH-functionalized cellulose fibrils, were first subjected to amine functionalization using poly(ethylene imine) (PEI). This chemical treatment relied on hydrogen bonding interactions between the OH groups of the cotton textiles and the NH_2 groups of the PEI. This treatment facilitated the direct deposition of metal nanoparticles (NPs) onto the cotton textiles via a ligand exchange reaction. The bulky native ligands of the metal NPs were replaced by the outermost NH_2 groups of the cotton textile surfaces, which had a higher affinity for the metal NPs. Following a similar adsorption mechanism, metal NPs (such as Au or Ag NPs) and small diethylenetriamine (DETA) molecules were alternately deposited on the amine-functionalized substrates by covalent bonding interaction. This process imparted electrical conductivity to insulating cotton textiles. Notably, the metal NP layers sandwiched between adjacent DETA layers were free of bulky organic ligands. This structural design minimized the separation distance (i.e., contact resistance) between adjacent metal NPs (Figure 8b). In this case, the sheet resistance of the $(\text{metal NP/DETA})_4$-deposited cotton textiles was measured to be approximately 650 Ω sq^{-1}, which was considered suitable for the electroplating process. Subsequently, the Ni electroplating process was performed on the $(\text{metal NP/DETA})_4$-deposited cotton textiles, which further reduced the sheet resistance to 0.05 Ω sq^{-1}. The resulting electroplated Ni-cotton textile (referred to as EP Ni-cotton) exhibited complete and uniform coverage, with the EP Ni layer extending from the outer surface to the central region, and no metal agglomeration was observed. Importantly, the EP Ni cotton served as a highly efficient HER electrode, exhibiting remarkably low overpotentials of 12 mV at 10 mA cm^{-2}, while also acting as an effective host electrode. In addition, the EP-Ni cotton facilitated the uniform incorporation of transition metal

https://doi.org/10.1021/acsmaterialslett.4c00659
ACS Materials Lett. 2024, 6, 3133−3160

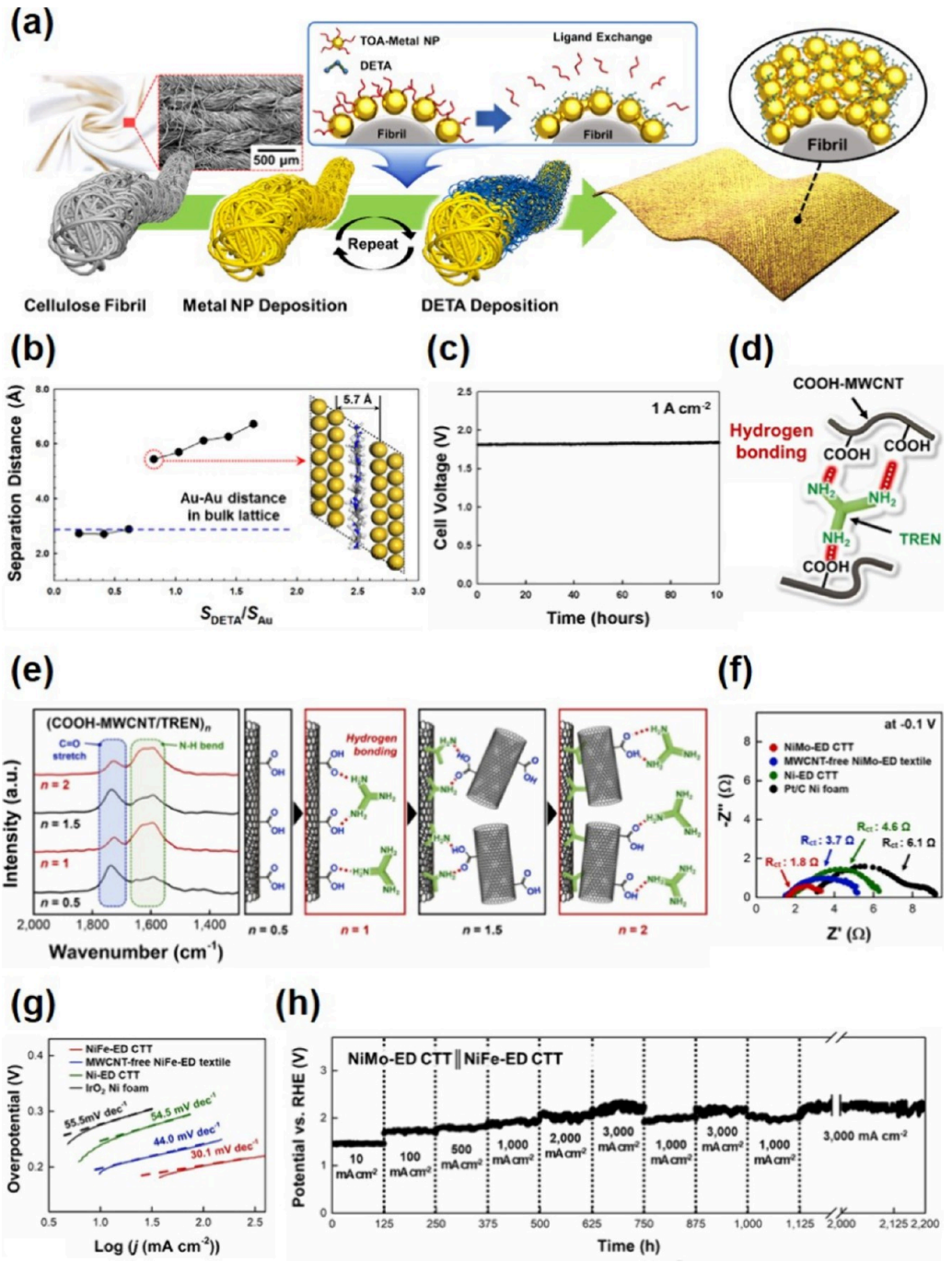

Figure 8. (a) Schematic illustration of the conductive cotton for water-splitting electrocatalysts based on the metal NP assembly driven electroplating approach. Reproduced with permission from ref 146. Copyright 2021, Wiley-VCH. (b) The molecular dynamic (MD)-computed minimal distance between Au atomic surfaces separated by DETA molecules as a function of surface coverage ratio (S_{DETA}/S_{Au}). The blue dotted horizontal line shows the interparticle distance of Au−Au in the bulk lattice (2.884 Å). The image in the r.h.s. represents the MD-simulated molecular structure of DETAs between Au atomic surfaces at S_{DETA}/S_{Au} = 1.0. Reproduced with permission from ref 146. Copyright 2021, Wiley-VCH. (c) Chronopotentiometry curve of the EP Ni−cotton‖EP NiFe LDH/Ni-cotton electrode recorded at 1 A cm^{-2}. Reproduced with permission from ref 146. Copyright 2021, Wiley-VCH. (d) Schematic representation of carboxylic acid-functionalized multiwalled carbon nanotubes (COOH-MWCNTs) assembled with amine (NH_2)-functionalized molecular linkers via hydrogen bonding interactions. Reproduced with permission from ref 156. Copyright 2024, Elsevier. (e) FT-IR spectra of a (COOH-MWCNTs/TREN)n multilayer as a function of the bilayer number (n) and corresponding illustration of the cohesive mechanism. Reproduced with permission from ref 156. Copyright 2024, Elsevier. (f) EIS plots of NiMo-ED CTT, MWCNT-free NiMo-ED textile, Ni-ED CTT, and Pt/C Ni foam. EIS plots were measured at an applied potential of −0.1 V (vs. RHE). Reproduced with permission from ref 156. Copyright 2024, Elsevier. (g) Tafel plots of the NiFe-ED CTT, MWCNT-free NiFe-ED textile, Ni-ED CTT, and IrO_2 Ni foam. Reproduced with permission from ref 156. Copyright 2024, Elsevier. (h) Chronopotentiometry stability test of the NiMo-ED CTT‖NiFe-ED CTT electrodes recorded at 10 mA cm^{-2}, 100 mA cm^{-2}, 500 mA cm^{-2}, 1000 mA cm^{-2}, 2000 mA cm^{-2}, and 3000 mA cm^{-2}. Reproduced with permission from ref 156. Copyright 2024, Elsevier.

https://doi.org/10.1021/acsmaterialslett.4c00659
ACS Materials Lett. 2024, 6, 3133−3160

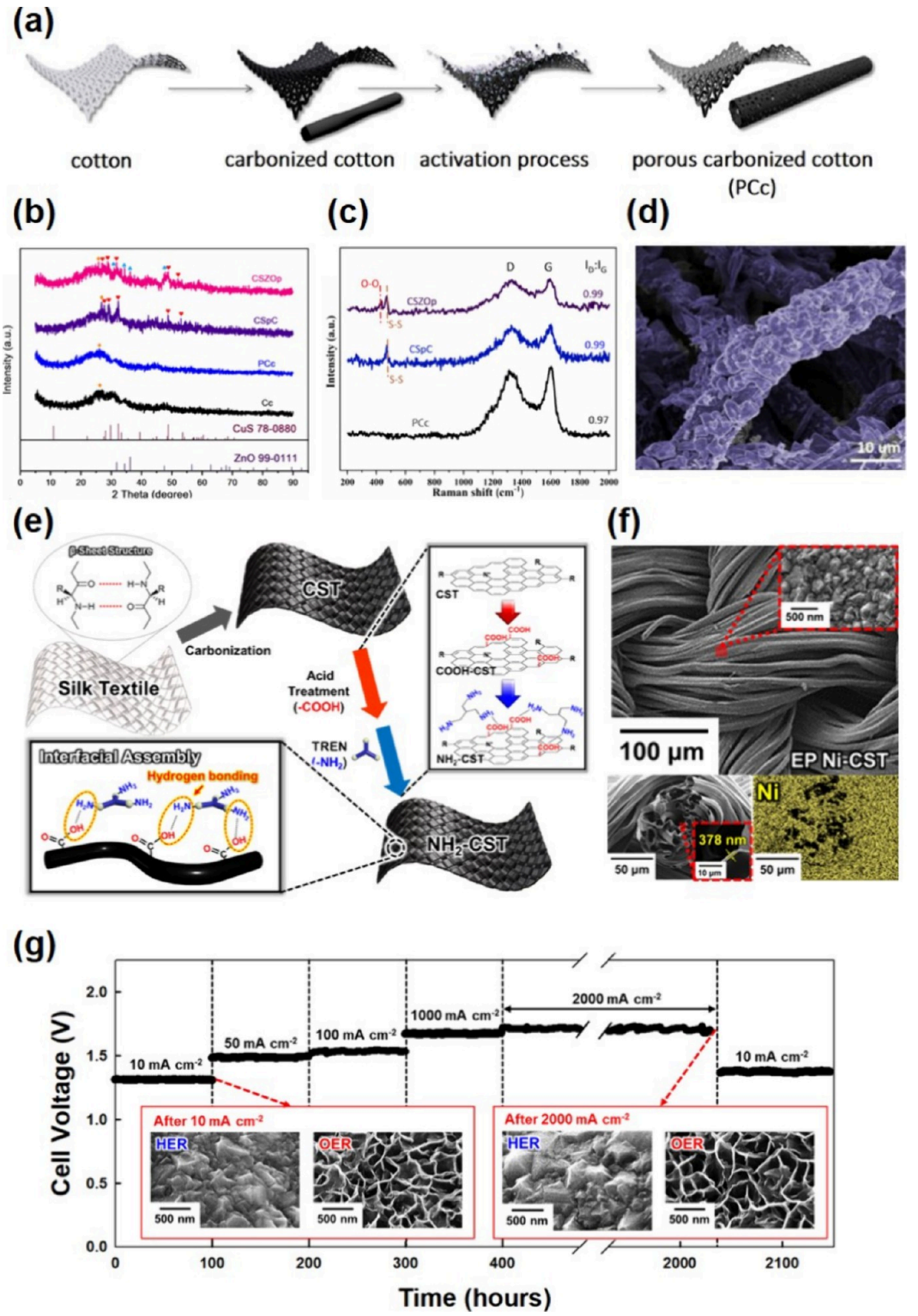

Figure 9. (a) Schematic diagram of the preparation process of PCc. Reprinted with permission from ref 158. Copyright 2021, Elsevier. (b) XRD patterns of CSZOp, CSpC, PCc and *Cc*. Reprinted with permission from ref 158. Copyright 2021, Elsevier. (c) Raman spectra of CSZOp, CSpC and PCc. Reprinted with permission from ref 158. Copyright 2021, Elsevier. (d) False-colored SEM image of CSpC. Reprinted with permission from ref 158. Copyright 2021, Elsevier. (e) Schematic illustration of the carbonization/interfacial assembly approach to fabricated textile-based water-splitting electrodes. Reproduced with permission from ref 159. Copyright 2022, The Royal Society of Chemistry. (f) FE-SEM images and energy-dispersive X-ray spectroscopy (EDX) mapping image of EP Ni-CST. The inset shows the surface morphology (top) and thickness of the EP Ni layer (bottom). Reproduced with permission from ref 159. Copyright 2022, The Royal Society of Chemistry. (g) Chronopotentiometry curves of the EP Ni-CST||EP NiFeCo-CST electrodes recorded at 10 mA cm^{-2}, 50 mA cm^{-2}, 100 mA cm^{-2}, 1000 mA cm^{-2}, and 2000 mA cm^{-2}. The inset shows the planar FE-SEM images of the EP Ni-CST||EP NiFeCo-CST electrodes after the stability test. Reproduced with permission from ref 159. Copyright 2022, The Royal Society of Chemistry.

https://doi.org/10.1021/acsmaterialslett.4c00659
ACS Materials Lett. 2024, 6, 3133−3160

electrocatalysts, such as NiFe, for OER electrode fabrication. Thanks to these innovative structural and interfacial design strategies, a full-cell device composed of EP Ni-cotton (serving as the cathode for HER) and NiFe LDH electroplated on the EP Ni-cotton (serving as the anode for OER) achieved an exceptionally low cell voltage of 1.39 V at 10 mA cm^{-2}. Moreover, the device exhibited excellent operational stability, maintaining constant cell voltages for 100 h at a high current density of 1 A cm^{-2} in 1 M KOH (Figure 8c). However, despite the high performance of these AWS textile electrodes using noble metal NPs as conductive seeds for electroplating non-noble metals such as Ni and NiFe, there is a pressing need for a more economical fabrication approach.

More recently, Son et al. introduced highly efficient AWS electrodes by using molecular linker assembly induced all-in-one structured binary transition metal electrocatalyst.[156] As shown in Figure 8d, carboxylic acid-functionalized multiwalled carbon nanotubes (COOH-MWCNTs) were assembled with amine (NH_2)-functionalized molecular linkers such as tris(2-aminoethyl)amine (TREN) via hydrogen bonding interactions in ethanol. This assembly resulted in the deposition of $(COOH\text{-}MWCNT/TREN)_n$ multilayers on TREN-coated cotton textiles, hereafter referred to as CTT. Fourier transform infrared (FT-IR) spectroscopy confirmed the increase in absorption peak intensities of the COOH and NH_2 groups with the bilayer number (n) of the multilayers (Figure 8e). In particular, due to the remarkably thin thickness of the TREN molecular linkers (about 5.6 Å),[151,157] the NH_2 groups of these linkers formed direct bridges between the interfaces of the cotton textiles and the COOH-MWCNTs, as well as between adjacent COOH-MWCNTs. As a result, the resulting $(COOH\text{-}MWCNT/TREN)_{20}$-coated textile exhibited a sheet resistance of $2.2 \times 10^3\ \Omega\ sq^{-1}$, which was later converted into a bulk metal-like host electrode for water-splitting electrocatalysts by Ni electrodeposition. This process reduced the sheet resistance to about $0.06\ \Omega\ sq^{-1}$. The Ni-electrodeposited $(COOH\text{-}MWCNT/TREN)_{20}$ multilayer coated textile, abbreviated as Ni-ED CTT, exhibited a significantly larger specific surface area of about 3.6 $m^2\ g^{-1}$ compared to the $(COOH\text{-}MWCNT/TREN)_{20}$ coated textile, which had a surface area of about 2.7 $m^2\ g^{-1}$, due to its unique nanoprotuberant structure. This difference in surface area had a profound effect on the available surface area for subsequent electrodeposited electrocatalysts, specifically NiMo for HER and NiFe for OER.

After undergoing successive electrodeposition processes to become NiMo-ED CTT for the HER electrode and NiFe-ED CTT for the OER electrode, these materials retained their distinctive properties, including porous structure, large specific surface area, high electrical conductivity, and mechanical stability. In particular, they exhibited remarkably low overpotentials of 8 mV at 10 mA cm^{-2} for HER and 189 mV at 50 mA cm^{-2} for OER. To elucidate these outstanding performances, a series of analyses including XPS, XANES, EXAFS, *operando* Raman spectroscopy and DFT calculations were performed to investigate the electron structure of the bimetallic electrocatalysts. These studies confirmed the occurrence of electron transfer between Ni and Mo or Fe, thereby optimizing the electron structure of the electrocatalysts. As a result, lower charge transfer resistances (R_{ct}) and Tafel slopes were observed compared to those of the Ni-ED CTT (Figure 8**f, g**). Utilizing these integrated design strategies with stable host electrodes and potent electrocatalysts, a full-cell device composed of the NiMo-ED CTT and the NiFe-ED CTT demonstrated exceptional performance, achieving low cell voltages of 2.01 V at a high current density of 3000 mA cm^{-2}. Remarkably, cell voltages remained constant for at least 2000 h at current densities ranging from 10 to 3000 mA cm^{-2} (Figure 8h).

As mentioned in the previous section, the carbonization process is another promising method for converting insulating textiles into conductive ones by forming polyaromatic structures within the textile. However, this process transforms the hydrophilic surface of pristine textile into a hydrophobic one due to the formation of aromatic carbon structures. Consequently, a major challenge for carbonized textile host electrodes lies in balancing high electrical properties with hydrophilicity. This balance is essential for uniformly depositing electrocatalysts and facilitating mass transfer in aqueous solutions.

To this end, Zhai et al. recently proposed an activated carbonized cotton host electrode, denoted as PCc, for use in an OER electrode under alkaline media (Figure 9a).[158] The process involved immersing a carbonized cotton textile (*Cc*) in a KOH solution (with a mass ratio of *Cc* to KOH at about 1:2), followed by heating the immersed *Cc* to 800 °C to activate its surface and improve the ion transport efficiency of the *Cc*. The XRD analysis confirmed that both *Cc* and PCc exhibited the diffraction peaks around 25.9° attributed to the (002) plane of amorphous graphite, indicating the preservation of the polyaromatic structures after the activation process. In addition, Raman spectroscopy revealed the characteristic peaks at 1332 and 1594 cm^{-1}, corresponding to structural defects (D-band) and the crystalline hexagonal lattice (G-band) of graphitic carbon, respectively (Figure 9**b, c**). Subsequently, the prepared PCc current collector (i.e., host electrode) was immersed in a $CuSO_4$ solution to absorb Cu^{2+} ions sequentially, followed by immersion in a Na_2S solution to absorb S^{2-} ions and initiate their reaction with Cu^{2+}. The resulting CuS layer was effectively deposited onto the surface of activated fibers without agglomeration (Figure 9d). This substrate, termed CuS/PCc composite (CSpC), was further transformed into a CuS/ZnO/PCc (CSZOp) electrode using vacuum thermal evaporation technology (VTET) with CSpC and ZnO NPs. The incorporation of ZnO NPs significantly reduced the bandgap energy and enhanced the electrical conductivity of the CuS composite, thereby lowering the RDS energy barrier. Consequently, the CSZOp exhibited a low overpotential of 337 mV at a current density of 10 mA cm^{-2} and a remarkably low Tafel slope of 58.2 mV dec^{-1}.

To advance the development of much more stable carbonized textile-based electrodes at high current densities, Mo et al. introduced a carbonization/interfacial assembly driven electroplating approach using natural silk textiles (Figure 9e).[159] Silk textiles possess β-sheet-rich protein structures, which transform into sp^2-hybridized carbon hexagonal structures starting at 300 °C and eventually form highly ordered graphitic structures. In their study, this unique pyrolysis behavior of silk textiles resulted in carbonized silk textiles (CSTs) with high electrical conductivity (~4.3 S cm^{-1}) and low sheet resistance (~6.6 $\Omega\ sq^{-1}$) at 950 °C. After carbonization, acid treatment and subsequent attachment of amine groups using TREN molecules were performed to enhance the affinity with transition metal-based electrocatalysts via covalent bonding interaction. In addition, the outermost hydrophilic amine groups facilitated the uniform deposition of electrocatalysts over the entire area of the CSTs, from the

https://doi.org/10.1021/acsmaterialslett.4c00659
ACS Materials Lett. 2024, 6, 3133−3160

inside to the outside, and accelerated the reduction of metal ions in the electrocatalytic components (Figure 9f). An electrocatalytic Ni layer was uniformly electroplated on the amine-attached CST (referred to as NH_2−CST), forming a protuberant structure with a low sheet resistance of 0.05 Ω sq^{-1}.

Moreover, the Ni electroplated CST (EP-CST) maintained its initial electrical conductivity even after mechanical bending cycle testing due to its meticulously engineered interface. In particular, as already mentioned above, the EP-CST served not only as a bulk metal-like conductive host electrode with an extremely large specific surface area, but also as a highly efficient HER electrode in AWS, exhibiting a considerably low overpotential of 12 mV at 10 mA cm^{-2}, coupled with a low Tafel slope of about 31.8 mV dec^{-1}. For the preparation of OER electrode, a NiFeCo layer was additionally electroplated on the EP Ni-CST, yielding a highly uniform and distinctive wrinkled-nanostructure. The resulting NiFeCo-CST OER electrode also exhibited remarkable OER performance with a low overpotential of about 186 mV at 50 mA cm^{-2} and a low Tafel slope of about 30.9 mV dec^{-1}. To further confirm the crucial structural and electrochemical effects of the electrocatalysts in both HER and OER, the authors performed thorough analyses employing high-resolution transmission electron microscopy (HR-TEM), Raman spectroscopy, XRD, XPS, and DFT calculations. These investigations evidently revealed the physical/chemical structures and electronic binding energies, which facilitate the adsorption/desorption of intermediate reactants during the water-splitting reaction. Due to the remarkable interfacial design of all electrode components, a full-cell device composed of Ni-CST and NiFeCo-CST showed exceptional stability over extended operation periods, lasting at least >1640 h, even under an extremely high current density of 2000 mA cm^{-2} (Figure 9g).

Although noble metals such as Pt, Ir, and Ru exhibit superior electrocatalytic performance compared to catalysts based on non-noble metals, it is important to recognize that the meticulous structural and interfacial design of transition metal alloy-based water-splitting electrodes, featuring electron-modulated properties and extremely large active surface area, can achieve the electrocatalytic performance comparable to noble metals. Additionally, these electrodes demonstrate excellent operational stability, making them well suited for application in commercial electrolysis systems.

As described in this perspective, research on advanced water-splitting electrodes is critical to realizing carbon neutrality in emerging societies. However, it is very difficult to achieve the theoretical properties of active electrocatalysts without proper structural and interfacial design of the electrodes because the core of this challenge strongly depends on the effective design of the interfaces among all electrode components, where numerous electrical/electrochemical events occur, and the structural design of electrodes for large electrocatalytic area, as well as the development of high-performance non-noble electrocatalysts. Although the use of highly efficient electrocatalytic nanomaterials in the water-splitting reaction can provide significant advantages such as an extremely large active surface area, this also means an increase in the number of interfaces between individual components (i.e., electrocatalytic NPs and/or host electrode), which can increase the internal resistance and lead to electrocatalytic instability problems. In addition, the internal resistance of the electrode can be more pronounced due to the presence of insulating organic species (i.e., polymeric binders, surfactants, and organic ligands) adsorbed on the surface of the electrocatalytic nanomaterials. Therefore, to achieve reliable output performance, the separation distance (i.e., internal resistance) and interfacial interaction between adjacent component materials within the electrode should be meticulously tailored by an appropriate interfacial design. Furthermore, to realize mechanically robust water-splitting electrodes under the high gas bubble pressure that occurs during the high-current-density-induced water-splitting reaction, the mismatch in interfacial interaction between the electrocatalytic components and the host electrode, as well as between adjacent electrocatalytic nanomaterials must be resolved.

The effective electroplating of non-noble electrocatalysts onto textile-based host electrode with large surface area and bulk metal-like electrical conductivity can produce high-performance alkaline water-splitting electrodes, enabling extremely low overpotentials and long-term operational stability even under high current densities, which is in stark contrast with conventional electrodes prepared through chemical reduction and slurry casting methods. Moreover, the uniform coating and stable adsorption of all-in-one structured electrocatalysts onto conductive textiles effectively preserve both the internal porous structure and mechanically flexible properties of the pristine textile substrates. These factors directly impact the output performance of alkaline water-splitting electrodes. Thus, comprehensive electrode design considerations, spanning from host electrode to electrocatalysts, are essential for enhancing water-splitting electrode performance.

However, despite these significant advances in high-performance water-splitting electrodes, several critical issues remain to be addressed. Particularly, among notable approaches that can be used to prepare the high-quality textile host electrodes, a LbL assembly of conductive components has some issues to be solved in terms of mass production and turnaround time for commercialization. Although a few approaches based on rapid automated deposition techniques (e.g., spin coating and spray deposition) have been applied to address these issues, such techniques, in the case of using hydrophobic NPs as conductive components, are not effective in completely eliminating the native hydrophobic ligands bounds to the surface of metal NPs during short washing time as well as in depositing the conductive components onto 3D porous substrates instead of 2D-flat substrates. Although carbonization approach can also be considered as a promising candidate in that it is very simple, fast, and efficient in converting from insulating natural textiles into conductive textile host electrodes, it should be noted that the carbonization approach has limited applicability to protein or cellulose-based silk textiles, except for nylon and polyester-based textiles which show a high degree of brittleness at the carbonization temperature (>600 °C). On the other hand, a coating approach, such as a roll-to-roll deposition process, which can effectively wash out the weakly adsorbed species including hydrophobic ligands through a controllable immersion time, may be an alternative approach.[160] This method is applicable to mass production of film-type host electrodes irrespective of substrate shapes.

In view of non-noble electrocatalysts for high-performance alkaline water-splitting electrodes, it is highly desirable that they should have larger active surface area through nanosized control. However, one of the most critical issues in such

https://doi.org/10.1021/acsmaterialslett.4c00659
ACS Materials Lett. 2024, 6, 3133−3160

nanosized electrocatalysts is their unstable adsorption (i.e., electrocatalytic instability) onto the host electrode as already mentioned above. Although the uniform electroplating of all-in-one structured non-noble electrocatalysts onto the textile host electrodes with extremely large surface area can significantly enhance the active surface area and operational stability of overall electrode, the better effective approach may be the direct, dense, and robust adsorption of the nanosized electrocatalysts onto textile host electrodes without electrochemically inactive components. Therefore, if the synthesis of intrinsically highly efficient electrocatalysts, the assembly process based on favorable interfacial interactions, and the overall electrode design with large active surface area can be integrally and deeply considered for developing the water-splitting electrodes, they can provide important insights for realizing the high-performance HER and OER electrodes with lower overpotentials (or low cell voltages for full-cell device) and more excellent operational stability at high current densities compared to alkaline electrodes reported to date.

AUTHOR INFORMATION

Corresponding Authors

Dongsoo Yang − *Department of Chemical and Biological Engineering, Korea University, Seongbuk-gu, Seoul 02841, Republic of Korea;* orcid.org/0000-0002-0299-3128; Email: dosoyang@korea.ac.kr

Jinhan Cho − *Department of Chemical and Biological Engineering and KU-KIST Graduate School of Converging Science and Technology, Korea University, Seongbuk-gu, Seoul 02841, Republic of Korea; Soft Hybrid Materials Research Center, Advanced Materials Research Division, Korea Institute of Science and Technology (KIST), Seongbuk-gu, Seoul 02792, Republic of Korea;* orcid.org/0000-0002-7097-5968; Email: jinhan71@korea.ac.kr

Authors

Jeongmin Mo − *Department of Chemical and Biological Engineering, Korea University, Seongbuk-gu, Seoul 02841, Republic of Korea;* orcid.org/0000-0001-8375-1974

Wondo Choi − *Department of Chemical and Biological Engineering, Korea University, Seongbuk-gu, Seoul 02841, Republic of Korea;* orcid.org/0000-0001-7279-6712

Hyaemin Kim − *Department of Chemical and Biological Engineering, Korea University, Seongbuk-gu, Seoul 02841, Republic of Korea;* orcid.org/0000-0003-2587-3476

Jaesung Lyu − *Department of Chemical and Biological Engineering, Korea University, Seongbuk-gu, Seoul 02841, Republic of Korea;* orcid.org/0009-0002-9870-3558

Cheong Hoon Kwon − *Department of Energy Resources and Chemical Engineering, Kangwon National University, Samcheok 25913, Republic of Korea;* orcid.org/0000-0002-9516-0669

Complete contact information is available at: https://pubs.acs.org/10.1021/acsmaterialslett.4c00659

Author Contributions

¶J.M. and W.C. contributed equally to this work. The manuscript was written through contributions of all authors. CRediT: **Jeongmin Mo** conceptualization, data curation, formal analysis, investigation, methodology, visualization, writing-original draft; **Wondo Choi** formal analysis, investigation, methodology, validation, visualization, writing-original draft; **Hyaemin Kim** investigation, methodology; **Jaesung Lyu** formal analysis, investigation, methodology; **Cheong Hoon Kwon** formal analysis, methodology; **Dongsoo Yang** formal analysis, investigation, methodology, writing-original draft; **Jinhan Cho** conceptualization, data curation, formal analysis, funding acquisition, investigation, methodology, resources, supervision, validation, visualization, writing-original draft, writing-review & editing.

Notes

The authors declare no competing financial interest.

Biographies

Jeongmin Mo is a Ph.D. candidate under Prof. Jinhan Cho at the Department of Chemical and Biological Engineering in Korea University. Currently, her research interest has focused on the fabrication of electrocatalysts for hydrogen evolution reaction (HER), oxygen evolution reaction (OER) and overall water splitting.

Wondo Choi is a Ph.D. candidiate under Prof. Jinhan Cho at Department of Chemical and Biological Engineering in Korea University. His current research topic is fabrication of HER/OER electrodes to water electrolysis in acidic media.

Hyaemin Kim is a M.S candidate under Prof. Jinhan Cho at the Department of Chemical and Biological Engineering in Korea University. Currently, her research interest encompasses the development of efficient electrocatalyst fabrication of HER/OER electrodes of water splitting in alkaline media based on Layer-by-Layer Assembly.

https://doi.org/10.1021/acsmaterialslett.4c00659
ACS Materials Lett. 2024, 6, 3133−3160

Jaesung Lyu is a Ph.D. candidate under Prof. Jinhan Cho at the Department of Chemical and Biological Engineering in Korea University. Currently, his research topic is related to the development of efficient electrocatalyst fabrication of HER/OER electrodes in water splitting method in alkaline media, based on Layer-by-Layer Assembly.

Cheong Hoon Kwon is a professor at the Department of Energy Resources and Chemical Engineering, Kangwon National University since 2022. She received her Ph.D. degree at the Department of Chemical and Biological Engineering in Korea University in 2008 and completed a postdoctoral program at Harvard Medical School in Boston (in 2009–2010). Her research has focused on the development of energy electrodes for applications in energy harvesting, conversion, and electrochemical sensing devices.

Dongsoo Yang is an assistant professor at the Department of Chemical & Biological Engineering in Korea University since 2022. He received his Ph.D. degree from KAIST in 2020. He continued to work at KAIST as a postdoctoral fellow until 2022. He is currently interested in enzyme engineering, development of synthetic biology tools for biomedical applications as well as the development of engineered bacteria for diagnostic or therapeutic purposes.

Jinhan Cho is a professor at the Department of Chemical & Biological Engineering in Korea University since 2010. His research career started in POSTECH and Seoul National University, where he completed M.S. and Ph.D. degrees in 1997 and 2001, respectively. He had postdoc courses at Max Planck Institute of Colloids and Interfaces (2001–2002). His research has focused on investigating the surface and electrochemistry of textile electrodes, developing their use in energy conversion and storage.

■ ACKNOWLEDGMENTS

This work was supported by a National Research Foundation of Korea (NRF) grant funded by the Korea government (Ministry of Science and ICT) (NRF-2021R1A2C3004151 and 2022R1A2C1009690). This work was also support from the KIST Institutional Program (Project No.: 2 V09840-23-P025) and the KU-KIST Graduate School of Converging Science and Technology Program.

■ REFERENCES

(1) Turner, J. A. Sustainable Hydrogen Production. *Science* **2004**, *305*, 972–974.
(2) Turner, J. A. A Realizable Renewable Energy Future. *Science* **1999**, *285*, 687–689.
(3) Fang, M.; Dong, G.; Wei, R.; Ho, J. C. Hierarchical Nanostructures: Design for Sustainable Water Splitting. *Adv. Energy Mater.* **2017**, *7*, No. 1700559.
(4) Guo, J.; Zheng, Y.; Hu, Z.; Zheng, C.; Mao, J.; Du, K.; Jaroniec, M.; Qiao, S.-Z.; Ling, T. Direct seawater electrolysis by adjusting the local reaction environment of a catalyst. *Nat. Energy* **2023**, *8*, 264–272.
(5) Roger, I.; Shipman, M. A.; Symes, M. D. Earth-abundant catalysts for electrochemical and photoelectrochemical water splitting. *Nat. Rev. Chem.* **2017**, *1*, 0003.
(6) Wang, Z.; Li, C.; Domen, K. Recent developments in heterogeneous photocatalysts for solar-driven overall water splitting. *Chem. Soc. Rev.* **2019**, *48*, 2109–2125.
(7) Tong, W.; Forster, M.; Dionigi, F.; Dresp, S.; Sadeghi Erami, R.; Strasser, P.; Cowan, A. J.; Farràs, P. Electrolysis of low-grade and saline surface water. *Nat. Energy* **2020**, *5*, 367–377.
(8) Zhang, W.; Liu, M.; Gu, X.; Shi, Y.; Deng, Z.; Cai, N. Water Electrolysis toward Elevated Temperature: Advances, Challenges and Frontiers. *Chem. Rev.* **2023**, *123*, 7119–7192.
(9) David, M.; Ocampo-Martínez, C.; Sánchez-Peña, R. Advances in alkaline water electrolyzers: A review. *J. Energy Storage* **2019**, *23*, 392–403.
(10) Younas, M.; Shafique, S.; Hafeez, A.; Javed, F.; Rehman, F. An Overview of Hydrogen Production: Current Status, Potential, and Challenges. *Fuel* **2022**, *316*, No. 123317.
(11) Singh, T. I.; Rajeshkhanna, G.; Pan, U. N.; Kshetri, T.; Lin, H.; Kim, N. H.; Lee, J. H. Alkaline Water Splitting Enhancement by MOF-Derived Fe–Co–Oxide/Co@NC-mNS Heterostructure: Boosting OER and HER through Defect Engineering and In Situ Oxidation. *Small* **2021**, *17*, No. 2101312.

https://doi.org/10.1021/acsmaterialslett.4c00659
ACS Materials Lett. 2024, 6, 3133–3160

(12) Wang, J.; Gao, Y.; Kong, H.; Kim, J.; Choi, S.; Ciucci, F.; Hao, Y.; Yang, S.; Shao, Z.; Lim, J. Non-precious-metal catalysts for alkaline water electrolysis: operando characterizations, theoretical calculations, and recent advances. *Chem. Soc. Rev.* **2020**, *49*, 9154−9196.
(13) Chung, D. Y.; Lopes, P. P.; Farinazzo Bergamo Dias Martins, P.; He, H.; Kawaguchi, T.; Zapol, P.; You, H.; Tripkovic, D.; Strmcnik, D.; Zhu, Y.; Seifert, S.; Lee, S.; Stamenkovic, V. R.; Markovic, N. M. Dynamic stability of active sites in hydr(oxy)oxides for the oxygen evolution reaction. *Nat. Energy* **2020**, *5*, 222−230.
(14) Shi, Y.; Zhou, S.; Liu, J.; Zhang, X.; Yin, J.; Zhan, T.; Yang, Y.; Li, G.; Lai, J.; Wang, L. An integrated amorphous cobalt phosphoselenide electrocatalyst with high mass activity boosts alkaline overall water splitting. *Appl. Catal. B: Environ.* **2024**, *341*, No. 123326.
(15) Wang, S.; Yuan, C.-Z.; Zheng, Y.; Kang, Y.; Hui, K. S.; Wang, K.; Gao, H.; Dinh, D. A.; Cho, Y.-R.; Hui, K. N. Boosting the Bifunctionality and Durability of Cobalt-Fluoride-Oxide Nanosheets for Alkaline Water Splitting Through Nitrogen-Plasma-Promoted Electronic Regulation and Structural Reconstruction. *ACS Catal.* **2024**, *14*, 3616−3626.
(16) Hu, Y.; Xiong, T.; Balogun, M. S. J. T.; Huang, Y.; Adekoya, D.; Zhang, S.; Tong, Y. Enhanced metallicity boosts hydrogen evolution capability of dual-bimetallic Ni−Fe nitride nanoparticles. *Mater. Today Phys.* **2020**, *15*, No. 100267.
(17) Yu, F.; Zhou, H.; Huang, Y.; Sun, J.; Qin, F.; Bao, J.; Goddard, W. A.; Chen, S.; Ren, Z. High-performance bifunctional porous non-noble metal phosphide catalyst for overall water splitting. *Nat. Commun.* **2018**, *9*, 2551.
(18) Lindquist, G. A.; Xu, Q.; Oener, S. Z.; Boettcher, S. W. Membrane Electrolyzers for Impure-Water Splitting. *Joule* **2020**, *4*, 2549−2561.
(19) Kou, T.; Wang, S.; Li, Y. Perspective on High-Rate Alkaline Water Splitting. *ACS Mater. Lett.* **2021**, *3*, 224−234.
(20) Buttler, A.; Spliethoff, H. Current status of water electrolysis for energy storage, grid balancing and sector coupling via power-to-gas and power-to-liquids: A review. *Renew. Sust. Energy Rev.* **2018**, *82*, 2440−2454.
(21) Schmidt, O.; Gambhir, A.; Staffell, I.; Hawkes, A.; Nelson, J.; Few, S. Future cost and performance of water electrolysis: An expert elicitation study. *Int. J. Hydrogen Energy* **2017**, *42*, 30470−30492.
(22) Luo, Y.; Zhang, Z.; Chhowalla, M.; Liu, B. Recent Advances in Design of Electrocatalysts for High-Current-Density Water Splitting. *Adv. Mater.* **2022**, *34*, No. 2108133.
(23) Ren, Q.; Feng, L.; Ye, C.; Xue, X.; Lin, D.; Eisenberg, S.; Kou, T.; Duoss, E. B.; Zhu, C.; Li, Y. Nanocone-Modified Surface Facilitates Gas Bubble Detachment for High-Rate Alkaline Water Splitting. *Adv. Energy Mater.* **2023**, *13*, No. 2302073.
(24) Long, X.; Lin, H.; Zhou, D.; An, Y.; Yang, S. Enhancing Full Water-Splitting Performance of Transition Metal Bifunctional Electrocatalysts in Alkaline Solutions by Tailoring CeO_2−Transition Metal Oxides−Ni Nanointerfaces. *ACS Energy Lett.* **2018**, *3*, 290−296.
(25) Zhang, Z.; Liu, S.; Xiao, F.; Wang, S. Facile Synthesis of Heterostructured Nickel/Nickel Oxide Wrapped Carbon Fiber: Flexible Bifunctional Gas-Evolving Electrode for Highly Efficient Overall Water Splitting. *ACS Sustainable Chem. Eng.* **2017**, *5*, 529−536.
(26) Suryanto, B. H. R.; Wang, Y.; Hocking, R. K.; Adamson, W.; Zhao, C. Overall electrochemical splitting of water at the heterogeneous interface of nickel and iron oxide. *Nat. Commun.* **2019**, *10*, 5599.
(27) Guo, W.; Yang, T.; Zhang, H.; Zhou, H.; Wei, W.; Liang, W.; Zhou, Y.; Yu, T.; Zhao, H. Charge-counterbalance modulated amorphous nickel oxide for efficient alkaline hydrogen and oxygen evolution. *Chem. Eng. J.* **2023**, *470*, No. 144241.
(28) Diao, F.; Huang, W.; Ctistis, G.; Wackerbarth, H.; Yang, Y.; Si, P.; Zhang, J.; Xiao, X.; Engelbrekt, C. Bifunctional and Self-Supported NiFeP-Layer-Coated NiP Rods for Electrochemical Water Splitting in Alkaline Solution. *ACS Appl. Mater. Interfaces* **2021**, *13*, 23702−23713.
(29) Fu, C.; Hao, W.; Fan, J.; Zhang, Q.; Guo, Y.; Fan, J.; Chen, Z.; Li, G. Fabrication of Ultra-Durable and Flexible NiP_x-Based Electrode toward High-Efficient Alkaline Seawater Splitting at Industrial Grade Current Density. *Small* **2023**, *19*, No. 2205689.
(30) Liang, Q.; Zhong, L.; Du, C.; Luo, Y.; Zhao, J.; Zheng, Y.; Xu, J.; Ma, J.; Liu, C.; Li, S.; Yan, Q. Interfacing Epitaxial Dinickel Phosphide to 2D Nickel Thiophosphate Nanosheets for Boosting Electrocatalytic Water Splitting. *ACS Nano* **2019**, *13*, 7975−7984.
(31) Singh, S.; Nguyen, D. C.; Kim, N. H.; Lee, J. H. Interface engineering induced electrocatalytic behavior in core-shelled CNTs@ NiP_2/NbP heterostructure for highly efficient overall water splitting. *Chem. Eng. J.* **2022**, *442*, No. 136120.
(32) Ma, W.; Li, D.; Liao, L.; Zhou, H.; Zhang, F.; Zhou, X.; Mo, Y.; Yu, F. High-Performance Bifunctional Porous Iron-Rich Phosphide/Nickel Nitride Heterostructures for Alkaline Seawater Splitting. *Small* **2023**, *19*, No. 2207082.
(33) Jia, J.; Zhai, M.; Lv, J.; Zhao, B.; Du, H.; Zhu, J. Nickel Molybdenum Nitride Nanorods Grown on Ni Foam as Efficient and Stable Bifunctional Electrocatalysts for Overall Water Splitting. *ACS Appl. Mater. Interfaces* **2018**, *10*, 30400−30408.
(34) Dutta, S.; Indra, A.; Feng, Y.; Han, H.; Song, T. Promoting electrocatalytic overall water splitting with nanohybrid of transition metal nitride-oxynitride. *Appl. Catal. B: Environ.* **2019**, *241*, 521−527.
(35) Ren, J.-T.; Wang, Y.-S.; Song, Y.-J.; Chen, L.; Yuan, Z.-Y. Interface engineering of in−situ formed nickel hydr(oxy)oxides on nickel nitrides to boost alkaline hydrogen electrocatalysis. *Appl. Catal. B: Environ.* **2022**, *309*, No. 121279.
(36) Chen, G.-F.; Ma, T. Y.; Liu, Z.-Q.; Li, N.; Su, Y.-Z.; Davey, K.; Qiao, S.-Z. Efficient and Stable Bifunctional Electrocatalysts Ni/Ni_xM_y (M = P, S) for Overall Water Splitting. *Adv. Funct. Mater.* **2016**, *26*, 3314−3323.
(37) Dang, J.; Yin, M.; Pan, D.; Tian, Z.; Chen, G.; Zou, J.; Miao, H.; Wang, Q.; Yuan, J. Four-functional iron/copper sulfide heterostructure for alkaline hybrid zinc batteries and water splitting. *Chem. Eng. J.* **2023**, *457*, No. 141357.
(38) Zhou, F.; Zhang, X.; Sa, R.; Zhang, S.; Wen, Z.; Wang, R. The electrochemical overall water splitting promoted by MoS_2 in coupled nickel−iron (oxy)hydride/molybdenum sulfide/graphene composite. *Chem. Eng. J.* **2020**, *397*, No. 125454.
(39) Hegazy, M. B. Z.; Zander, J.; Weiss, M.; Simon, C.; Gerschel, P.; Sanden, S. A.; Smialkowski, M.; Tetzlaff, D.; Kull, T.; Marschall, R.; Apfel, U.-P. $FeNi_2S_4$−A Potent Bifunctional Efficient Electrocatalyst for the Overall Electrochemical Water Splitting in Alkaline Electrolyte. *Small* **2024**, No. 2311627.
(40) Hao, S.; Chen, L.; Yu, C.; Yang, B.; Li, Z.; Hou, Y.; Lei, L.; Zhang, X. NiCoMo Hydroxide Nanosheet Arrays Synthesized via Chloride Corrosion for Overall Water Splitting. *ACS Energy Lett.* **2019**, *4*, 952−959.
(41) Luo, X.; Ji, P.; Wang, P.; Cheng, R.; Chen, D.; Lin, C.; Zhang, J.; He, J.; Shi, Z.; Li, N.; Xiao, S.; Mu, S. Interface Engineering of Hierarchical Branched Mo-Doped Ni_3S_2/Ni_xP_y Hollow Heterostructure Nanorods for Efficient Overall Water Splitting. *Adv. Energy Mater.* **2020**, *10*, No. 1903891.
(42) Li, Y.; Wei, B.; Yu, Z.; Bondarchuk, O.; Araujo, A.; Amorim, I.; Zhang, N.; Xu, J.; Neves, I. C.; Liu, L. Bifunctional Porous Cobalt Phosphide Foam for High-Current-Density Alkaline Water Electrolysis with 4000-h Long Stability. *ACS Sustainable Chem. Eng.* **2020**, *8*, 10193−10200.
(43) Lu, Z.; Zhu, W.; Yu, X.; Zhang, H.; Li, Y.; Sun, X.; Wang, X.; Wang, H.; Wang, J.; Luo, J.; Lei, X.; Jiang, L. Ultrahigh Hydrogen Evolution Performance of Under-Water "Superaerophobic" MoS_2 Nanostructured Electrodes. *Adv. Mater.* **2014**, *26*, 2683−2687.
(44) Xu, Y.; Wang, C.; Huang, Y.; Fu, J. Recent advances in electrocatalysts for neutral and large-current-density water electrolysis. *Nano Energy* **2021**, *80*, No. 105545.
(45) Wen, Q.; Zhao, Y.; Liu, Y.; Li, H.; Zhai, T. Ultrahigh-Current-Density and Long-Term-Durability Electrocatalysts for Water Splitting. *Small* **2022**, *18*, No. 2104513.

https://doi.org/10.1021/acsmaterialslett.4c00659
ACS Materials Lett. 2024, 6, 3133−3160

(46) Zhou, Q.; Liao, L.; Zhou, H.; Li, D.; Tang, D.; Yu, F. Innovative strategies in design of transition metal-based catalysts for large-current-density alkaline water/seawater electrolysis. *Mater. Today Phys.* **2022**, *26*, No. 100727.
(47) Chen, L.; Wang, Y.; Zhao, X.; Wang, Y.; Li, Q.; Wang, Q.; Tang, Y.; Lei, Y. Trimetallic oxyhydroxides as active sites for large-current-density alkaline oxygen evolution and overall water splitting. *J. Mater. Sci. Technol.* **2022**, *110*, 128−135.
(48) Yao, D.; Gu, L.; Zuo, B.; Weng, S.; Deng, S.; Hao, W. A strategy for preparing high-efficiency and economical catalytic electrodes toward overall water splitting. *Nanoscale* **2021**, *13*, 10624−10648.
(49) Sahasrabudhe, A.; Dixit, H.; Majee, R.; Bhattacharyya, S. Value added transformation of ubiquitous substrates into highly efficient and flexible electrodes for water splitting. *Nat. Commun.* **2018**, *9*, 2014.
(50) Liu, L.; Yu, Y.; Yan, C.; Li, K.; Zheng, Z. Wearable energy-dense and power-dense supercapacitor yarns enabled by scalable graphene−metallic textile composite electrodes. *Nat. Commun.* **2015**, *6*, 7260.
(51) Lee, H. M.; Choi, S.-Y.; Jung, A.; Ko, S. H. Highly conductive aluminum textile and paper for flexible and wearable electronics. *Angew. Chem., Int. Ed.* **2013**, *52*, 7718−7723.
(52) Li, M.; Xie, P.; Yu, L.; Luo, L.; Sun, X. Bubble Engineering on Micro-/Nanostructured Electrodes for Water Splitting. *ACS Nano* **2023**, *17*, 23299−23316.
(53) Yu, X.; Yu, Z.-Y.; Zhang, X.-L.; Zheng, Y.-R.; Duan, Y.; Gao, Q.; Wu, R.; Sun, B.; Gao, M.-R.; Wang, G.; Yu, S.-H. Superaerophobic" Nickel Phosphide Nanoarray Catalyst for Efficient Hydrogen Evolution at Ultrahigh Current Densities. *J. Am. Chem. Soc.* **2019**, *141*, 7537−7543.
(54) Han, N.; Yang, K. R.; Lu, Z.; Li, Y.; Xu, W.; Gao, T.; Cai, Z.; Zhang, Y.; Batista, V. S.; Liu, W.; Sun, X. Nitrogen-doped tungsten carbide nanoarray as an efficient bifunctional electrocatalyst for water splitting in acid. *Nat. Commun.* **2018**, *9*, 924.
(55) Hu, C.; Zhang, L.; Gong, J. Recent progress made in the mechanism comprehension and design of electrocatalysts for alkaline water splitting. *Energy Environ. Sci.* **2019**, *12*, 2620−2645.
(56) Sun, H.; Yan, Z.; Liu, F.; Xu, W.; Cheng, F.; Chen, J. Self-Supported Transition-Metal-Based Electrocatalysts for Hydrogen and Oxygen Evolution. *Adv. Mater.* **2020**, *32*, No. 1806326.
(57) Li, X.; Hao, X.; Abudula, A.; Guan, G. Nanostructured catalysts for electrochemical water splitting: current state and prospects. *J. Mater. Chem. A* **2016**, *4*, 11973−12000.
(58) Mahmood, N.; Yao, Y.; Zhang, J.-W.; Pan, L.; Zhang, X.; Zou, J.-J. Electrocatalysts for Hydrogen Evolution in Alkaline Electrolytes: Mechanisms, Challenges, and Prospective Solutions. *Adv. Sci.* **2018**, *5*, No. 1700464.
(59) Anantharaj, S.; Noda, S. Amorphous Catalysts and Electrochemical Water Splitting: An Untold Story of Harmony. *Small* **2020**, *16*, No. 1905779.
(60) Xie, X.; Du, L.; Yan, L.; Park, S.; Qiu, Y.; Sokolowski, J.; Wang, W.; Shao, Y. Oxygen Evolution Reaction in Alkaline Environment: Material Challenges and Solutions. *Adv. Funct. Mater.* **2022**, *32*, No. 2110036.
(61) Li, Z.; Zhang, X.; Ou, C.; Zhang, Y.; Wang, W.; Dong, S.; Dong, X. Transition metal-based self-supported anode for electrocatalytic water splitting at a large current density. *Coord. Chem. Rev.* **2023**, *495*, No. 215381.
(62) Yu, Z.-Y.; Duan, Y.; Feng, X.-Y.; Yu, X.; Gao, M.-R.; Yu, S.-H. Clean and Affordable Hydrogen Fuel from Alkaline Water Splitting: Past, Recent Progress, and Future Prospects. *Adv. Mater.* **2021**, *33*, No. 2007100.
(63) Hua, D.; Huang, J.; Fabbri, E.; Rafique, M.; Song, B. Development of Anion Exchange Membrane Water Electrolysis and the Associated Challenges: A Review. *ChemElectroChem.* **2023**, *10*, No. e202200999.
(64) Jin, H.; Ruqia, B.; Park, Y.; Kim, H. J.; Oh, H.-S.; Choi, S.-I.; Lee, K. Nanocatalyst Design for Long-Term Operation of Proton/Anion Exchange Membrane Water Electrolysis. *Adv. Energy Mater.* **2021**, *11*, No. 2003188.
(65) Xu, Q.; Zhang, L.; Zhang, J.; Wang, J.; Hu, Y.; Jiang, H.; Li, C. Anion Exchange Membrane Water Electrolyzer: Electrode Design, Lab-Scaled Testing System and Performance Evaluation. *EnergyChem.* **2022**, *4*, No. 100087.
(66) Rozain, C.; Millet, P. Electrochemical characterization of Polymer Electrolyte Membrane Water Electrolysis Cells. *Electrochim. Acta* **2014**, *131*, 160−167.
(67) Hodges, A.; Hoang, A. L.; Tsekouras, G.; Wagner, K.; Lee, C.-Y.; Swiegers, G. F.; Wallace, G. G. A high-performance capillary-fed electrolysis cell promises more cost-competitive renewable hydrogen. *Nat. Commun.* **2022**, *13*, 1304.
(68) Yu, F.; Yu, L.; Mishra, I. K.; Yu, Y.; Ren, Z. F.; Zhou, H. Q. Recent developments in earth-abundant and non-noble electrocatalysts for water electrolysis. *Mater. Today Phys.* **2018**, *7*, 121−138.
(69) Govind Rajan, A.; Martirez, J. M. P.; Carter, E. A. Why Do We Use the Materials and Operating Conditions We Use for Heterogeneous (Photo)Electrochemical Water Splitting? *ACS Catal.* **2020**, *10*, 11177−11234.
(70) Zhang, H.; Maijenburg, A. W.; Li, X.; Schweizer, S. L.; Wehrspohn, R. B. Bifunctional Heterostructured Transition Metal Phosphides for Efficient Electrochemical Water Splitting. *Adv. Funct. Mater.* **2020**, *30*, No. 2003261.
(71) Strmcnik, D.; Lopes, P. P.; Genorio, B.; Stamenkovic, V. R.; Markovic, N. M. Design principles for hydrogen evolution reaction catalyst materials. *Nano Energy* **2016**, *29*, 29−36.
(72) Huang, C.-L.; Lin, Y.-G.; Chiang, C.-L.; Peng, C.-K.; Senthil Raja, D.; Hsieh, C.-T.; Chen, Y.-A.; Chang, S.-Q.; Yeh, Y.-X.; Lu, S.-Y. Atomic scale synergistic interactions lead to breakthrough catalysts for electrocatalytic water splitting. *Appl. Catal. B: Environ.* **2023**, *320*, No. 122016.
(73) Jiao, Y.; Zheng, Y.; Jaroniec, M.; Qiao, S. Z. Design of electrocatalysts for oxygen- and hydrogen-involving energy conversion reactions. *Chem. Soc. Rev.* **2015**, *44*, 2060−2086.
(74) Luo, Y.; Guan, Y.; Liu, G.; Wang, Y.; Li, J.; Ricardez-Sandoval, L. First-Principles-Based Kinetic Monte Carlo Model of Hydrogen Evolution Reaction under Realistic Conditions: Solvent, Hydrogen Coverage and Electric Field Effects. *ACS Catal.* **2024**, *14*, 2696−2708.
(75) Li, J.; Stenlid, J. H.; Ludwig, T.; Lamoureux, P. S.; Abild-Pedersen, F. Modeling Potential-Dependent Electrochemical Activation Barriers: Revisiting the Alkaline Hydrogen Evolution Reaction. *J. Am. Chem. Soc.* **2021**, *143*, 19341−19355.
(76) Jadhav, H. S.; Bandal, H. A.; Ramakrishna, S.; Kim, H. Critical Review, Recent Updates on Zeolitic Imidazolate Framework-67 (ZIF-67) and Its Derivatives for Electrochemical Water Splitting. *Adv. Mater.* **2022**, *34*, No. 2107072.
(77) Anantharaj, S.; Ede, S. R.; Sakthikumar, K.; Karthick, K.; Mishra, S.; Kundu, S. Recent Trends and Perspectives in Electrochemical Water Splitting with an Emphasis on Sulfide, Selenide, and Phosphide Catalysts of Fe, Co, and Ni: A Review. *ACS Catal.* **2016**, *6*, 8069−8097.
(78) Anantharaj, S.; Kundu, S. Do the Evaluation Parameters Reflect Intrinsic Activity of Electrocatalysts in Electrochemical Water Splitting? *ACS Energy Lett.* **2019**, *4*, 1260−1264.
(79) Trasatti, S. Work function, electronegativity, and electrochemical behaviour of metals: II. Potentials of zero charge and "electrochemical" work functions. *J. Electroanal. Chem.* **1971**, *33*, 351−378.
(80) Zeradjanin, A. R.; Grote, J.-P.; Polymeros, G.; Mayrhofer, K. J. J. A Critical Review on Hydrogen Evolution Electrocatalysis: Re-exploring the Volcano-relationship. *Electroanalysis* **2016**, *28*, 2256−2269.
(81) Nørskov, J. K.; Bligaard, T.; Hvolbæk, B.; Abild-Pedersen, F.; Chorkendorff, I.; Christensen, C. H. The nature of the active site in heterogeneous metal catalysis. *Chem. Soc. Rev.* **2008**, *37*, 2163−2171.
(82) Greeley, J.; Jaramillo, T. F.; Bonde, J.; Chorkendorff, I.; Nørskov, J. K. Computational high-throughput screening of electro-

catalytic materials for hydrogen evolution. *Nat. Mater.* **2006**, *5*, 909−913.
(83) Sheng, W.; Myint, M.; Chen, J. G.; Yan, Y. Correlating the hydrogen evolution reaction activity in alkaline electrolytes with the hydrogen binding energy on monometallic surfaces. *Energy Environ. Sci.* **2013**, *6*, 1509−1512.
(84) Liu, F.; Shi, C.; Guo, X.; He, Z.; Pan, L.; Huang, Z.-F.; Zhang, X.; Zou, J.-J. Rational Design of Better Hydrogen Evolution Electrocatalysts for Water Splitting: A Review. *Adv. Sci.* **2022**, *9*, No. 2200307.
(85) Suen, N.-T.; Hung, S.-F.; Quan, Q.; Zhang, N.; Xu, Y.-J.; Chen, H. M. Electrocatalysis for the oxygen evolution reaction: recent development and future perspectives. *Chem. Soc. Rev.* **2017**, *46*, 337−365.
(86) Song, F.; Bai, L.; Moysiadou, A.; Lee, S.; Hu, C.; Liardet, L.; Hu, X. Transition Metal Oxides as Electrocatalysts for the Oxygen Evolution Reaction in Alkaline Solutions: An Application-Inspired Renaissance. *J. Am. Chem. Soc.* **2018**, *140*, 7748−7759.
(87) Grimaud, A.; Diaz-Morales, O.; Han, B.; Hong, W. T.; Lee, Y.-L.; Giordano, L.; Stoerzinger, K. A.; Koper, M. T. M.; Shao-Horn, Y. Activating lattice oxygen redox reactions in metal oxides to catalyse oxygen evolution. *Nat. Chem.* **2017**, *9*, 457−465.
(88) Zhang, N.; Chai, Y. Lattice oxygen redox chemistry in solid-state electrocatalysts for water oxidation. *Energy Environ. Sci.* **2021**, *14*, 4647−4671.
(89) Zhang, Y.; Fu, Q.; Song, B.; Xu, P. Regulation Strategy of Transition Metal Oxide-Based Electrocatalysts for Enhanced Oxygen Evolution Reaction. *Acc. Mater. Res.* **2022**, *3*, 1088−1100.
(90) Gao, L.; Cui, X.; Sewell, C. D.; Li, J.; Lin, Z. Recent advances in activating surface reconstruction for the high-efficiency oxygen evolution reaction. *Chem. Soc. Rev.* **2021**, *50*, 8428−8469.
(91) Zhou, D.; Li, P.; Lin, X.; McKinley, A.; Kuang, Y.; Liu, W.; Lin, W.-F.; Sun, X.; Duan, X. Layered double hydroxide-based electrocatalysts for the oxygen evolution reaction: identification and tailoring of active sites, and superaerophobic nanoarray electrode assembly. *Chem. Soc. Rev.* **2021**, *50*, 8790−8817.
(92) Yoo, J. S.; Rong, X.; Liu, Y.; Kolpak, A. M. Role of Lattice Oxygen Participation in Understanding Trends in the Oxygen Evolution Reaction on Perovskites. *ACS Catal.* **2018**, *8*, 4628−4636.
(93) Al-Naggar, A. H.; Shinde, N. M.; Kim, J.-S.; Mane, R. S. Water splitting performance of metal and non-metal-doped transition metal oxide electrocatalysts. *Coord. Chem. Rev.* **2023**, *474*, No. 214864.
(94) Jin, H.; Liu, X.; Chen, S.; Vasileff, A.; Li, L.; Jiao, Y.; Song, L.; Zheng, Y.; Qiao, S.-Z. Heteroatom-Doped Transition Metal Electrocatalysts for Hydrogen Evolution Reaction. *ACS Energy Lett.* **2019**, *4*, 805−810.
(95) Xu, H.; Jia, H.; Fei, B.; Ha, Y.; Li, H.; Guo, Y.; Liu, M.; Wu, R. Charge Transfer Engineering via Multiple Heteroatom Doping in Dual Carbon-Coupled Cobalt Phosphides for Highly Efficient Overall Water Splitting. *Appl. Catal. B: Environ.* **2020**, *268*, No. 118404.
(96) Zhang, J.; Xu, Q.; Wang, J.; Li, Y.; Jiang, H.; Li, C. Dual-defective Co_3O_4 nanoarrays enrich target intermediates and promise high-efficient overall water splitting. *Chem. Eng. J.* **2021**, *424*, No. 130328.
(97) Ding, Y.; Zhao, J.; Zhang, W.; Zhang, J.; Chen, X.; Yang, F.; Zhang, X. Single-Walled Carbon Nanotubes Wrapped $CoFe_2O_4$ Nanorods with Enriched Oxygen Vacancies for Efficient Overall Water Splitting. *ACS Appl. Energy Mater.* **2019**, *2*, 1026−1032.
(98) Zhang, T.; Wu, M.-Y.; Yan, D.-Y.; Mao, J.; Liu, H.; Hu, W.-B.; Du, X.-W.; Ling, T.; Qiao, S.-Z. Engineering oxygen vacancy on NiO nanorod arrays for alkaline hydrogen evolution. *Nano Energy* **2018**, *43*, 103−109.
(99) Zhao, Y.; Chang, C.; Teng, F.; Zhao, Y.; Chen, G.; Shi, R.; Waterhouse, G. I. N.; Huang, W.; Zhang, T. Defect-Engineered Ultrathin δ-MnO_2 Nanosheet Arrays as Bifunctional Electrodes for Efficient Overall Water Splitting. *Adv. Energy Mater.* **2017**, *7*, No. 1700005.
(100) Luo, Z.; Miao, R.; Huan, T. D.; Mosa, I. M.; Poyraz, A. S.; Zhong, W.; Cloud, J. E.; Kriz, D. A.; Thanneeru, S.; He, J.; Zhang, Y.; Ramprasad, R.; Suib, S. L. Mesoporous MoO_{3-x} Material as an Efficient Electrocatalyst for Hydrogen Evolution Reactions. *Adv. Energy Mater.* **2016**, *6*, No. 1600528.
(101) Huang, L.; Chen, D.; Luo, G.; Lu, Y.-R.; Chen, C.; Zou, Y.; Dong, C.-L.; Li, Y.; Wang, S. Zirconium-Regulation-Induced Bifunctionality in 3D Cobalt−Iron Oxide Nanosheets for Overall Water Splitting. *Adv. Mater.* **2019**, *31*, No. 1901439.
(102) Li, X.; Wang, Y.; Wang, J.; Da, Y.; Zhang, J.; Li, L.; Zhong, C.; Deng, Y.; Han, X.; Hu, W. Sequential Electrodeposition of Bifunctional Catalytically Active Structures in MoO_3/Ni−NiO Composite Electrocatalysts for Selective Hydrogen and Oxygen Evolution. *Adv. Mater.* **2020**, *32*, No. 2003414.
(103) Fan, G.; Li, F.; Evans, D. G.; Duan, X. Catalytic applications of layered double hydroxides: recent advances and perspectives. *Chem. Soc. Rev.* **2014**, *43*, 7040−7066.
(104) Yi, H.; Liu, S.; Lai, C.; Zeng, G.; Li, M.; Liu, X.; Li, B.; Huo, X.; Qin, L.; Li, L.; Zhang, M.; Fu, Y.; An, Z.; Chen, L. Recent Advance of Transition-Metal-Based Layered Double Hydroxide Nanosheets: Synthesis, Properties, Modification, and Electrocatalytic Applications. *Adv. Energy Mater.* **2021**, *11*, No. 2002863.
(105) Sahoo, D. P.; Das, K. K.; Mansingh, S.; Sultana, S.; Parida, K. Recent progress in first row transition metal Layered double hydroxide (LDH) based electrocatalysts towards water splitting: A review with insights on synthesis. *Coord. Chem. Rev.* **2022**, *469*, No. 214666.
(106) Anantharaj, S.; Karthick, K.; Kundu, S. Evolution of layered double hydroxides (LDH) as high performance water oxidation electrocatalysts: A review with insights on structure, activity and mechanism. *Mater. Today Energy* **2017**, *6*, 1−26.
(107) Jeghan, S. M. N.; Kim, D.; Lee, Y.; Kim, M.; Lee, G. Designing a smart heterojunction coupling of cobalt-iron layered double hydroxide on nickel selenide nanosheets for highly efficient overall water splitting kinetics. *Appl. Catal. B: Environ.* **2022**, *308*, No. 121221.
(108) Zhou, Q.; Chen, Y.; Zhao, G.; Lin, Y.; Yu, Z.; Xu, X.; Wang, X.; Liu, H. K.; Sun, W.; Dou, S. X. Active-Site-Enriched Iron-Doped Nickel/Cobalt Hydroxide Nanosheets for Enhanced Oxygen Evolution Reaction. *ACS Catal.* **2018**, *8*, 5382−5390.
(109) Li, P.; Duan, X.; Kuang, Y.; Li, Y.; Zhang, G.; Liu, W.; Sun, X. Tuning Electronic Structure of NiFe Layered Double Hydroxides with Vanadium Doping toward High Efficient Electrocatalytic Water Oxidation. *Adv. Energy Mater.* **2018**, *8*, No. 1703341.
(110) Liu, P.; Rodriguez, J. A. Catalysts for Hydrogen Evolution from the [NiFe] Hydrogenase to the $Ni_2P(001)$ Surface: The Importance of Ensemble Effect. *J. Am. Chem. Soc.* **2005**, *127*, 14871−14878.
(111) Xu, Y.; Wu, R.; Zhang, J.; Shi, Y.; Zhang, B. Anion-exchange synthesis of nanoporous FeP nanosheets as electrocatalysts for hydrogen evolution reaction. *Chem. Commun.* **2013**, *49*, 6656−6658.
(112) Popczun, E. J.; McKone, J. R.; Read, C. G.; Biacchi, A. J.; Wiltrout, A. M.; Lewis, N. S.; Schaak, R. E. Nanostructured Nickel Phosphide as an Electrocatalyst for the Hydrogen Evolution Reaction. *J. Am. Chem. Soc.* **2013**, *135*, 9267−9270.
(113) Weng, C.-C.; Ren, J.-T.; Yuan, Z.-Y. Transition Metal Phosphide-Based Materials for Efficient Electrochemical Hydrogen Evolution: A Critical Review. *ChemSusChem* **2020**, *13*, 3357−3375.
(114) Du, H.; Kong, R.-M.; Guo, X.; Qu, F.; Li, J. Recent progress in transition metal phosphides with enhanced electrocatalysis for hydrogen evolution. *Nanoscale* **2018**, *10*, 21617−21624.
(115) Wang, Y.; Kong, B.; Zhao, D.; Wang, H.; Selomulya, C. Strategies for developing transition metal phosphides as heterogeneous electrocatalysts for water splitting. *Nano Today* **2017**, *15*, 26−55.
(116) Yang, M.; Jiang, Y.; Qu, M.; Qin, Y.; Wang, Y.; Shen, W.; He, R.; Su, W.; Li, M. Strong electronic couple engineering of transition metal phosphides-oxides heterostructures as multifunctional electrocatalyst for hydrogen production. *Appl. Catal. B: Environ.* **2020**, *269*, No. 118803.

https://doi.org/10.1021/acsmaterialslett.4c00659
ACS Materials Lett. 2024, 6, 3133−3160

(117) Ji, L.; Wang, J.; Teng, X.; Meyer, T. J.; Chen, Z. CoP Nanoframes as Bifunctional Electrocatalysts for Efficient Overall Water Splitting. *ACS Catal.* **2020**, *10*, 412−419.
(118) Batool, M.; Hameed, A.; Nadeem, M. A. Recent developments on iron and nickel-based transition metal nitrides for overall water splitting: A critical review. *Coord. Chem. Rev.* **2023**, *480*, No. 215029.
(119) Peng, X.; Pi, C.; Zhang, X.; Li, S.; Huo, K.; Chu, P. K. Recent progress of transition metal nitrides for efficient electrocatalytic water splitting. *Sustainable Energy Fuels* **2019**, *3*, 366−381.
(120) Yang, H.-M.; Weng, C.-C.; Wang, H.-Y.; Yuan, Z.-Y. Transition metal nitride-based materials as efficient electrocatalysts: Design strategies and prospective applications. *Coord. Chem. Rev.* **2023**, *496*, No. 215410.
(121) Wen, Y.; Qi, J.; Wei, P.; Kang, X.; Li, X. Design of Ni_3N/Co_2N heterojunctions for boosting electrocatalytic alkaline overall water splitting. *J. Mater. Chem. A* **2021**, *9*, 10260−10269.
(122) Chen, M.; Liu, D.; Zi, B.; Chen, Y.; Liu, D.; Du, X.; Li, F.; Zhou, P.; Ke, Y.; Li, J.; Lo, K. H.; Kwok, C. T.; Ip, W. F.; Chen, S.; Wang, S.; Liu, Q.; Pan, H. Remarkable synergistic effect in cobalt-iron nitride/alloy nanosheets for robust electrochemical water splitting. *J. Energy Chem.* **2022**, *65*, 405−414.
(123) Zhao, Y.; Wei, S.; Pan, K.; Dong, Z.; Zhang, B.; Wu, H.-H.; Zhang, Q.; Lin, J.; Pang, H. Self-supporting transition metal chalcogenides on metal substrates for catalytic water splitting. *Chem. Eng. J.* **2021**, *421*, No. 129645.
(124) Chandra Majhi, K.; Karfa, P.; Madhuri, R. Bimetallic transition metal chalcogenide nanowire array: An effective catalyst for overall water splitting. *Electrochim. Acta* **2019**, *318*, 901−912.
(125) Zhang, J.; Wang, T.; Pohl, D.; Rellinghaus, B.; Dong, R.; Liu, S.; Zhuang, X.; Feng, X. Interface Engineering of MoS_2/Ni_3S_2 Heterostructures for Highly Enhanced Electrochemical Overall-Water-Splitting Activity. *Angew. Chem., Int. Ed.* **2016**, *55*, 6702−6707.
(126) Zhang, T.; Song, F.; Wang, Y.; Yuan, J.; Niu, L.; Wang, A.-j.; Fang, K. Bifunctional WS_2@Co_3S_4 core-shell nanowire arrays for efficient water splitting. *Electrochim. Acta* **2022**, *404*, No. 139648.
(127) Li, Y.; Yin, J.; An, L.; Lu, M.; Sun, K.; Zhao, Y.-Q.; Gao, D.; Cheng, F.; Xi, P. FeS_2/CoS_2 Interface Nanosheets as Efficient Bifunctional Electrocatalyst for Overall Water Splitting. *Small* **2018**, *14*, No. 1801070.
(128) Li, M.; Qian, Y.; Du, J.; Wu, H.; Zhang, L.; Li, G.; Li, K.; Wang, W.; Kang, D. J. CuS Nanosheets Decorated with CoS_2 Nanoparticles as an Efficient Electrocatalyst for Enhanced Hydrogen Evolution at All pH Values. *ACS Sustainable Chem. Eng.* **2019**, *7*, 14016−14022.
(129) Zou, X.; Wu, Y.; Liu, Y.; Liu, D.; Li, W.; Gu, L.; Liu, H.; Wang, P.; Sun, L.; Zhang, Y. In Situ Generation of Bifunctional, Efficient Fe-Based Catalysts from Mackinawite Iron Sulfide for Water Splitting. *Chem.* **2018**, *4*, 1139−1152.
(130) Yin, J.; Jin, J.; Zhang, H.; Lu, M.; Peng, Y.; Huang, B.; Xi, P.; Yan, C.-H. Atomic Arrangement in Metal-Doped NiS_2 Boosts the Hydrogen Evolution Reaction in Alkaline Media. *Angew. Chem., Int. Ed.* **2019**, *58*, 18676−18682.
(131) Hinnemann, B.; Moses, P. G.; Bonde, J.; Jørgensen, K. P.; Nielsen, J. H.; Horch, S.; Chorkendorff, I.; Nørskov, J. K. Biomimetic Hydrogen Evolution: MoS_2 Nanoparticles as Catalyst for Hydrogen Evolution. *J. Am. Chem. Soc.* **2005**, *127*, 5308−5309.
(132) Zhang, G.; Feng, Y.-S.; Lu, W.-T.; He, D.; Wang, C.-Y.; Li, Y.-K.; Wang, X.-Y.; Cao, F.-F. Enhanced Catalysis of Electrochemical Overall Water Splitting in Alkaline Media by Fe Doping in Ni_3S_2 Nanosheet Arrays. *ACS Catal.* **2018**, *8*, 5431−5441.
(133) Zhang, F.; Wang, X.; Han, W.; Qian, Y.; Qiu, L.; He, Y.; Lei, L.; Zhang, X. The Synergistic Activation of Ce-Doping and CoP/Ni_3P Hybrid Interaction for Efficient Water Splitting at Large-Current-Density. *Adv. Funct. Mater.* **2023**, *33*, No. 2212381.
(134) Yuan, H.; Wang, S.; Gu, X.; Tang, B.; Li, J.; Wang, X. One-step solid-phase boronation to fabricate self-supported porous FeNiB/FeNi foam for efficient electrocatalytic oxygen evolution and overall water splitting. *J. Mater. Chem. A* **2019**, *7*, 19554−19564.
(135) Koutavarapu, R.; Venkata Reddy, C.; Babu, B.; Reddy, K. R.; Cho, M.; Shim, J. Carbon cloth/transition metals-based hybrids with controllable architectures for electrocatalytic hydrogen evolution - A review. *Int. J. Hydrogen Energy* **2020**, *45*, 7716−7740.
(136) Chen, Z.; Zheng, L.; Zhu, T.; Ma, Z.; Yang, Y.; Wei, C.; Liu, L.; Gong, X. All-Solid-State Flexible Asymmetric Supercapacitors Fabricated by the Binder-Free Hydrophilic Carbon Cloth@MnO_2 and Hydrophilic Carbon Cloth@Polypyrrole Electrodes. *Adv. Electron. Mater.* **2019**, *5*, No. 1800721.
(137) Eisa, T.; Mohamed, H. O.; Choi, Y.-J.; Park, S.-G.; Ali, R.; Abdelkareem, M. A.; Oh, S.-E.; Chae, K.-J. Nickel nanorods over nickel foam as standalone anode for direct alkaline methanol and ethanol fuel cell. *Int. J. Hydrogen Energy* **2020**, *45*, 5948−5959.
(138) Jost, K.; Perez, C. R.; McDonough, J. K.; Presser, V.; Heon, M.; Dion, G.; Gogotsi, Y. Carbon coated textiles for flexible energy storage. *Energy Environ. Sci.* **2011**, *4*, 5060−5067.
(139) Dong, K.; Peng, X.; Wang, Z. L. Fiber/Fabric-Based Piezoelectric and Triboelectric Nanogenerators for Flexible/Stretchable and Wearable Electronics and Artificial Intelligence. *Adv. Mater.* **2020**, *32*, No. 1902549.
(140) Chen, G.; Xiao, X.; Zhao, X.; Tat, T.; Bick, M.; Chen, J. Electronic Textiles for Wearable Point-of-Care Systems. *Chem. Rev.* **2022**, *122*, 3259−3291.
(141) Yao, B.; Zhang, J.; Kou, T.; Song, Y.; Liu, T.; Li, Y. Paper-Based Electrodes for Flexible Energy Storage Devices. *Adv. Sci.* **2017**, *4*, No. 1700107.
(142) Hao, W.; Wu, R.; Huang, H.; Ou, X.; Wang, L.; Sun, D.; Ma, X.; Guo, Y. Fabrication of practical catalytic electrodes using insulating and eco-friendly substrates for overall water splitting. *Energy Environ. Sci.* **2020**, *13*, 102−110.
(143) Cho, S. Y.; Yun, Y. S.; Lee, S.; Jang, D.; Park, K.-Y.; Kim, J. K.; Kim, B. H.; Kang, K.; Kaplan, D. L.; Jin, H.-J. Carbonization of a stable β-sheet-rich silk protein into a pseudographitic pyroprotein. *Nat. Commun.* **2015**, *6*, 7145.
(144) Jiang, E.; Song, N.; Hong, S.; Xiao, M.; Zhu, D.; Yan, Z.; Sun, J.; Chen, G.; Li, C.; Dong, H. Cobalt supported on biomass carbon tubes derived from cotton fibers towards high-efficient electrocatalytic overall water-splitting. *Electrochim. Acta* **2022**, *407*, No. 139895.
(145) Gong, T.; Zhang, J.; Liu, Y.; Hou, L.; Deng, J.; Yuan, C. Construction of hetero-phase Mo_2C-CoO@N-CNFs film as a self-supported Bi-functional catalyst towards overall water splitting. *Chem. Eng. J.* **2023**, *451*, No. 139025.
(146) Ko, Y.; Park, J.; Mo, J.; Lee, S.; Song, Y.; Ko, Y.; Lee, H.; Kim, Y.; Huh, J.; Lee, S. W.; Cho, J. Layer-by-Layer Assembly-Based Electrocatalytic Fibril Electrodes Enabling Extremely Low Overpotentials and Stable Operation at 1 A cm^{-2} in Water-Splitting Reaction. *Adv. Funct. Mater.* **2021**, *31*, No. 2102530.
(147) Caruso, F.; Caruso, R. A.; Möhwald, H. Nanoengineering of Inorganic and Hybrid Hollow Spheres by Colloidal Templating. *Science* **1998**, *282*, 1111−1114.
(148) Decher, G. Fuzzy Nanoassemblies: Toward Layered Polymeric Multicomposites. *Science* **1997**, *277*, 1232−1237.
(149) Kovtyukhova, N. I.; Ollivier, P. J.; Martin, B. R.; Mallouk, T. E.; Chizhik, S. A.; Buzaneva, E. V.; Gorchinskiy, A. D. Layer-by-Layer Assembly of Ultrathin Composite Films from Micron-Sized Graphite Oxide Sheets and Polycations. *Chem. Mater.* **1999**, *11*, 771−778.
(150) Cho, I.; Song, Y.; Cheong, S.; Kim, Y.; Cho, J. Layer-by-Layer Assembled Oxide Nanoparticle Electrodes with High Transparency, Electrical Conductivity, and Electrochemical Activity by Reducing Organic Linker-Induced Oxygen Vacancies. *Small* **2020**, *16*, No. 1906768.
(151) Kang, S.; Nam, D.; Choi, J.; Ko, J.; Kim, D.; Kwon, C. H.; Huh, J.; Cho, J. Highly Conductive Paper/Textile Electrodes Using Ligand Exchange Reaction-Induced in Situ Metallic Fusion. *ACS Appl. Mater. Interfaces* **2019**, *11*, 12032−12042.
(152) Chang, W.; Nam, D.; Lee, S.; Ko, Y.; Kwon, C. H.; Ko, Y.; Cho, J. Fibril-Type Textile Electrodes Enabling Extremely High Areal Capacity through Pseudocapacitive Electroplating onto Chalcogenide Nanoparticle-Encapsulated Fibrils. *Adv. Sci.* **2022**, *9*, No. 2203800.

https://doi.org/10.1021/acsmaterialslett.4c00659
ACS Materials Lett. 2024, 6, 3133−3160

(153) Song, Y.; Bae, W.; Ahn, J.; Son, Y.; Kwon, M.; Kwon, C. H.; Kim, Y.; Ko, Y.; Cho, J. Carbon Nanocluster-Mediated Nanoblending Assembly for Binder-Free Energy Storage Electrodes with High Capacities and Enhanced Charge Transfer Kinetics. *Adv. Sci.* **2023**, *10*, No. 2301248.
(154) Yoo, C.; Lee, S.; Song, Y.; Chang, W.; Park, M. K.; Ko, Y.; Cho, J. Micro/nano-wrinkled elastomeric electrodes enabling high energy storage performance and various form factors. *Carbon Energy* **2023**, *5*, No. e335.
(155) Kang, M.; Nam, D.; Ahn, J.; Chung, Y. J.; Lee, S. W.; Choi, Y.-B.; Kwon, C. H.; Cho, J. A Mediator-Free Multi-Ply Biofuel Cell Using an Interfacial Assembly between Hydrophilic Enzymes and Hydrophobic Conductive Oxide Nanoparticles with Pointed Apexes. *Adv. Mater.* **2023**, *35*, No. 2304986.
(156) Son, Y.; Mo, J.; Yong, E.; Ahn, J.; Kim, G.; Lee, W.; Kwon, C. H.; Ju, H.; Lee, S. W.; Kim, B.-H.; Kim, M.; Cho, J. Highly efficient water-splitting electrodes with stable operation at 3 A cm^{-2} in alkaline media through molecular linker assembly-induced all-in-one structured NiMo and NiFe electrocatalysts. *Appl. Catal. B: Environ.* **2024**, *343*, No. 123563.
(157) Ko, Y.; Kwon, C. H.; Lee, S. W.; Cho, J. Nanoparticle-Based Electrodes with High Charge Transfer Efficiency through Ligand Exchange Layer-by-Layer Assembly. *Adv. Mater.* **2020**, *32*, No. 2001924.
(158) Zhai, S.; Luo, Y.; Fan, Z.; Zhou, M.; Hou, K.; Zhao, H.; Hu, M.; Xiao, Y.; Jin, K.; Zhao, Y.; Li, X.; Cai, Z. Porous carbonized cotton loaded with Zn−Cu−M(M = O, S) nanocomposites for electrochemical energy storage and oxygen evolution reaction. *Mater. Today Energy* **2021**, *21*, No. 100806.
(159) Mo, J.; Ko, Y.; Yun, Y. S.; Huh, J.; Cho, J. A carbonization/interfacial assembly-driven electroplating approach for water-splitting textile electrodes with remarkably low overpotentials and high operational stability. *Energy Environ. Sci.* **2022**, *15*, 3815−3829.
(160) Richardson, J. J.; Cui, J.; Björnmalm, M.; Braunger, J. A.; Ejima, H.; Caruso, F. Innovation in Layer-by-Layer Assembly. *Chem. Rev.* **2016**, *116*, 14828−14867.
(161) Qayum, A.; Peng, X.; Yuan, J.; Qu, Y.; Zhou, J.; Huang, Z.; Xia, H.; Liu, Z.; Tan, D. Q.; Chu, P. K.; Lu, F.; Hu, L. Highly Durable and Efficient Ni-FeO_x/$FeNi_3$ Electrocatalysts Synthesized by a Facile In Situ Combustion-Based Method for Overall Water Splitting with Large Current Densities. *ACS Appl. Mater. interfaces* **2022**, *14*, 27842−27853.
(162) Ren, J.; Wang, Q.; Xiang, Q.; Yang, C.; Liang, Y.; Li, J.; Liu, J.; Qian, D. O-vacancy-rich and heterostructured Cu/Cu_2O/NiO@NiCu foam self-supported advanced electrocatalyst towards hydrogen evolution: An experimental and DFT study. *Chem. Eng. Sci.* **2023**, *280*, No. 119026.
(163) Zhou, M.; Zeng, Y.; Liu, Y.; Sun, Y.; Lu, F.; Zhang, X.; Cao, R.; Xue, Y.; Zeng, X.; Wu, Y. Ni-Mo based metal/oxide heterostructured nanosheets with largely exposed interfacial atoms for overall water-splitting. *Appl. Surf. Sci.* **2022**, *597*, No. 153597.
(164) Dhandapani, H. N.; Mahendiran, D.; Karmakar, A.; Devi, P.; Nagappan, S.; Madhu, R.; Bera, K.; Murugan, P.; Babu, B. R.; Kundu, S. Boosting of overall water splitting activity by regulating the electron distribution over the active sites of Ce doped NiCo−LDH and atomic level understanding of the catalyst by DFT study. *J. Mater. Chem. A* **2022**, *10*, 17488−17500.
(165) Tang, Y.; Liu, Q.; Dong, L.; Wu, H. B.; Yu, X.-Y. Activating the hydrogen evolution and overall water splitting performance of NiFe LDH by cation doping and plasma reduction. *Appl. Catal. B: Environ.* **2020**, *266*, No. 118627.
(166) Qiu, Z.; Tai, C.-W.; Niklasson, G. A.; Edvinsson, T. Direct observation of active catalyst surface phases and the effect of dynamic self-optimization in NiFe-layered double hydroxides for alkaline water splitting. *Energy Environ. Sci.* **2019**, *12*, 572−581.
(167) Xiong, L.; Wang, B.; Cai, H.; Hao, H.; Li, J.; Yang, T.; Yang, S. Understanding the doping effect on hydrogen evolution activity of transition-metal phosphides: Modeled with Ni_2P. *Appl. Catal. B: Environ.* **2021**, *295*, No. 120283.
(168) Liu, Y.; Zhang, Z.; Zhang, L.; Xia, Y.; Wang, H.; Liu, H.; Ge, S.; Yu, J. Manipulating the *d*-band centers of transition metal phosphides through dual metal doping towards robust overall water splitting. *J. Mater. Chem. A* **2022**, *10*, 22125−22134.
(169) Gu, Y.; Chen, S.; Ren, J.; Jia, Y. A.; Chen, C.; Komarneni, S.; Yang, D.; Yao, X. Electronic Structure Tuning in Ni_3FeN/r-GO Aerogel toward Bifunctional Electrocatalyst for Overall Water Splitting. *ACS Nano* **2018**, *12*, 245−253.
(170) Fei, B.; Chen, Z.; Liu, J.; Xu, H.; Yan, X.; Qing, H.; Chen, M.; Wu, R. Ultrathinning Nickel Sulfide with Modulated Electron Density for Efficient Water Splitting. *Adv. Energy Mater.* **2020**, *10*, No. 2001963.
(171) Chen, P.; Zhou, T.; Zhang, M.; Tong, Y.; Zhong, C.; Zhang, N.; Zhang, L.; Wu, C.; Xie, Y. 3D Nitrogen-Anion-Decorated Nickel Sulfides for Highly Efficient Overall Water Splitting. *Adv. Mater.* **2017**, *29*, No. 1701584.
(172) Chen, R.; Zhang, Z.; Wang, Z.; Wu, W.; Du, S.; Zhu, W.; Lv, H.; Cheng, N. Constructing Air-Stable and Reconstruction-Inhibited Transition Metal Sulfide Catalysts via Tailoring Electron-Deficient Distribution for Water Oxidation. *ACS Catal.* **2022**, *12*, 13234−13246.
(173) Yang, L.; Huang, L.; Yao, Y.; Jiao, L. In-situ construction of lattice-matching NiP_2/$NiSe_2$ heterointerfaces with electron redistribution for boosting overall water splitting. *Appl. Catal. B: Environ.* **2021**, *282*, No. 119584.
(174) Zang, Y.; Lu, D.-Q.; Wang, K.; Li, B.; Peng, P.; Lan, Y.-Q.; Zang, S.-Q. A pyrolysis-free Ni/Fe bimetallic electrocatalyst for overall water splitting. *Nat. Commun.* **2023**, *14*, 1792.
(175) Fan, J.; Wang, L.; Xiang, X.; Liu, Y.; Shi, N.; Lin, Y.; Xu, D.; Jiang, J.; Lai, Y.; Bao, J.; Han, M. Porous Flower-Like Nanoarchitectures Derived from Nickel Phosphide Nanocrystals Anchored on Amorphous Vanadium Phosphate Nanosheet Nanohybrids for Superior Overall Water Splitting. *Small Methods* **2024**, No. 2301279.
(176) Dutta, S.; Indra, A.; Feng, Y.; Song, T.; Paik, U. Self-Supported Nickel Iron Layered Double Hydroxide-Nickel Selenide Electrocatalyst for Superior Water Splitting Activity. *ACS Appl. Mater. Interfaces* **2017**, *9*, 33766−33774.
(177) Zheng, J.; Zhang, J.; Zhang, L.; Zhang, W.; Wang, X.; Cui, Z.; Song, H.; Liang, Z.; Du, L. Ultrafast Carbothermal Shock Constructing $Ni_3Fe_{1-x}Cr_x$ Intermetallic Integrated Electrodes for Efficient and Durable Overall Water Splitting. *ACS Appl. Mater. Interfaces* **2022**, *14*, 19524−19533.
(178) Zheng, X.; Chen, Y.; Bao, X.; Mao, S.; Fan, R.; Wang, Y. In Situ Formed Bimetallic Carbide Ni_6Mo_6C Nanodots and $NiMoO_x$ Nanosheet Array Hybrids Anchored on Carbon Cloth: Efficient and Flexible Self-Supported Catalysts for Hydrogen Evolution. *ACS Catal.* **2020**, *10*, 11634−11642.
(179) Yang, L.; Liu, R.; Jiao, L. Electronic Redistribution: Construction and Modulation of Interface Engineering on CoP for Enhancing Overall Water Splitting. *Adv. Funct. Mater.* **2020**, *30*, No. 1909618.
(180) Zhang, L.; Lei, Y.; Xu, W.; Wang, D.; Zhao, Y.; Chen, W.; Xiang, X.; Pang, X.; Zhang, B.; Shang, H. Highly active and durable nitrogen-doped CoP/CeO_2 nanowire heterostructures for overall water splitting. *Chem. Eng. J.* **2023**, *460*, No. 141119.
(181) Zhou, J.; Wang, Z.; Yang, D.; Qi, F.; Hao, X.; Zhang, W.; Chen, Y. $NiSe_2$-anchored N, S-doped graphene/Ni foam as a free-standing bifunctional electrocatalyst for efficient water splitting. *Nanoscale* **2020**, *12*, 9866−9872.
(182) Tan, L.; Yu, J.; Wang, H.; Gao, H.; Liu, X.; Wang, L.; She, X.; Zhan, T. Controllable synthesis and phase-dependent catalytic performance of dual-phase nickel selenides on Ni foam for overall water splitting. *Appl. Catal. B: Environ.* **2022**, *303*, No. 120915.
(183) Singha Roy, S.; Karmakar, A.; Madhu, R.; Nagappan, S.; N Dhandapani, H.; Kundu, S. Three-Dimensional Sm-Doped NiCu-LDH on Ni Foam as a Highly Robust Bifunctional Electrocatalyst for Total Water Splitting. *ACS Appl. Energy Mater.* **2023**, *6*, 8818−8829.
(184) Wang, P.; Luo, Y.; Zhang, G.; Chen, Z.; Ranganathan, H.; Sun, S.; Shi, Z. Interface Engineering of Ni_xS_y@MnO_xH_y Nanorods to

https://doi.org/10.1021/acsmaterialslett.4c00659
ACS Materials Lett. 2024, 6, 3133−3160

Efficiently Enhance Overall-Water-Splitting Activity and Stability. *Nano-Micro Lett.* **2022**, *14*, 120.
(185) Li, H.; Gao, X.; Li, G. Construction of Co_2P-Ni_3S_2/NF Heterogeneous Structural Hollow Nanowires as Bifunctional Electrocatalysts for Efficient Overall Water Splitting. *Small* **2023**, *19*, No. 2304081.
(186) Dong, Y.; Deng, Z.; Xu, Z.; Liu, G.; Wang, X. Synergistic Tuning of CoO/CoP Heterojunction Nanowire Arrays as Efficient Bifunctional Catalysts for Alkaline Overall Water Splitting. *Small Methods* **2023**, *7*, No. 2300071.
(187) Panda, C.; Menezes, P. W.; Zheng, M.; Orthmann, S.; Driess, M. In Situ Formation of Nanostructured Core−Shell Cu_3N−CuO to Promote Alkaline Water Electrolysis. *ACS Energy Lett.* **2019**, *4*, 747−754.
(188) Xu, B.; Chen, Z.; Yang, X.; Wang, X.; Huang, Y.; Li, C. Electronic modulation of carbon-encapsulated NiSe composites via Fe doping for synergistic oxygen evolution. *Chem. Commun.* **2018**, *54*, 9075−9078.
(189) Chen, H.; Hui, B. Flexible NiFeP@filter paper electrode for alkaline overall water electrosplitting. *Int. J. Hydrogen Energy* **2024**, *51*, 615−623.
(190) Rajan, H.; Christy, M.; Jothi, V. R.; Anantharaj, S.; Yi, S. C. A bifunctional hexa-filamentous microfibril multimetallic foam: an unconventional high-performance electrode for total water splitting under industrial operation conditions. *J. Mater. Chem. A* **2021**, *9*, 4971−4983.
(191) Amiinu, I. S.; Pu, Z.; He, D.; Monestel, H. G. R.; Mu, S. Scalable cellulose-sponsored functionalized carbon nanorods induced by cobalt for efficient overall water splitting. *Carbon* **2018**, *137*, 274−281.
(192) Ren, J.; Antonietti, M.; Fellinger, T.-P. Efficient Water Splitting Using a Simple Ni/N/C Paper Electrocatalyst. *Adv. Energy Mater.* **2015**, *5*, No. 1401660.
(193) Li, M.; Zhu, Y.; Wang, H.; Wang, C.; Pinna, N.; Lu, X. Ni Strongly Coupled with Mo_2C Encapsulated in Nitrogen-Doped Carbon Nanofibers as Robust Bifunctional Catalyst for Overall Water Splitting. *Adv. Energy Mater.* **2019**, *9*, No. 1803185.
(194) Sharma, P. J.; Modi, K. H.; Sahatiya, P.; Sumesh, C. K.; Pataniya, P. M. Electroless deposited NiP-fabric electrodes for efficient water and urea electrolysis for hydrogen production at industrial scale. *Appl. Surf. Sci.* **2024**, *644*, No. 158766.
(195) Zhou, Q.; Liu, Z.; Wang, X.; Li, Y.; Qin, X.; Guo, L.; Zhou, L.; Xu, W. Co_3S_4-pyrolysis lotus fiber flexible textile as a hybrid electrocatalyst for overall water splitting. *J. Energy Chem.* **2024**, *89*, 336−344.
(196) Thota, R.; Ganesh, V. High-Performance Electrocatalysts for Hydrogen Evolution Reaction Using Flexible Electrodes Made up of Chemically Modified Polyester Films. *ChemistrySelect* **2018**, *3*, 2738−2746.
(197) Jiang, S.; Shao, H.; Cao, G.; Li, H.; Xu, W.; Li, J.; Fang, J.; Wang, X. Waste cotton fabric derived porous carbon containing Fe_3O_4/NiS nanoparticles for electrocatalytic oxygen evolution. *J. Mater. Sci. Technol.* **2020**, *59*, 92−99.
(198) Zhang, Y.; Zhang, Z.; Zhang, X.; Gao, X.; Shang, Z.; Huang, X.; Guo, E.; Si, C.; Wei, M.; Lu, Q.; Han, X. Amorphous nanosphere self-supporting electrode based on filter paper for efficient water splitting. *J. Alloy. Compd.* **2024**, *972*, No. 172854.
(199) Wang, Z.; Ji, S.; Liu, F.; Wang, H.; Wang, X.; Wang, Q.; Pollet, B. G.; Wang, R. Highly Efficient and Stable Catalyst Based on $Co(OH)_2$@Ni Electroplated on Cu-Metallized Cotton Textile for Water Splitting. *ACS Appl. Mater. Interfaces* **2019**, *11*, 29791−29798.
(200) Sun, W.-H.; Hua, Y.-Q.; Zhang, X. Assembly of amorphous CoP electrocatalysts on flexible polyester textile for alkaline hydrogen evolution reaction. *Int. J. Hydrogen Energy* **2024**, *63*, 28−35.

https://doi.org/10.1021/acsmaterialslett.4c00659
ACS Materials Lett. 2024, 6, 3133−3160